SYNTHESIS OF ^{18}F-FLUORODEOXYSORBITOL FOR ASSESSMENT OF GLYMPHATIC CLEARANCE IN RATS

By

Katherine Brown

A THESIS

Submitted to
Michigan State University
in partial fulfillment of the requirements
for the degree of

Comparative Medicine and Integrative Biology - Master of Science

2024

ABSTRACT

The glymphatic system plays a critical role in waste clearance from the brain, and its dysfunction has been implicated in neurodegenerative diseases such as Alzheimer's. This thesis investigated the synthesis of ^{18}F-Fluorodeoxysorbitol (^{18}F-FDS) as a positron emission tomography (PET) tracer for assessing glymphatic clearance and compared different administration routes to identify the most effective and clinically translatable method.

The synthesis of ^{18}F-FDS from widely available ^{18}F-FDG was achieved through a simple reduction reaction and confirmed by high-performance liquid chromatography (HPLC). The product exhibited high stability and purity, making it a viable candidate for glymphatic imaging. PET imaging was employed to assess glymphatic clearance in both young and aged rat models following intrathecal (IT) and intranasal (IN) administration of ^{18}F-FDS. Results from IT administration in young animals showed significant clearance of the tracer, indicating rapid glymphatic activity, whereas aged animals exhibited severely diminished clearance, highlighting the age-related decline in this system.

The study also explored the potential of IN administration as a non-invasive alternative to IT injections. IN delivery through the nose-to-brain (N2B) pathway was compared to intravenous (IV) and IT administration, with IN showing the highest levels in the brain. Despite variability in early IN experiments, this method holds promise for clinical translation due to its non-invasive nature and desirable brain delivery.

^{18}F-FDS demonstrated significant potential as a PET tracer for glymphatic clearance studies, particularly in identifying age-related changes in brain function. Future research should focus on refining IN administration techniques and exploring its application in clinical settings for the early detection and monitoring of neurodegenerative diseases.

This thesis is dedicated to my husband, for his unwavering enthusiasm and constant support during late-night scientific pursuits.

ACKNOWLEDGEMENTS

First and foremost, I would like to express my deepest gratitude to my family, who believed in me even when I didn't believe in myself. To my parents, Jim and Bridget Rodgers, your unwavering support and encouragement have been my bedrock. To my grandparents, Kathy and Jim Rodgers, your wisdom and love have been a constant source of strength. My best friend, Brenna MacLeod, who is just as much family as those related by blood, thank you for always being there for me. To my husband, Colin Brown, your love and patience have been my guiding light throughout this journey. And to my beloved cats, Oscar and Bliss, who enthusiastically embraced their title of emotional support animals.

I am immensely grateful to my mentors and committee members who guided me and encouraged me to show what I am capable of. Dr. Colleen Hegg, thank you for answering my countless questions with patience and expertise. Dr. Jinda Fan, your kindness and dedication in guiding me through challenging chemistry has been invaluable. Dr. David Morgan, your belief in my abilities pushed me to strive for excellence. Dr. Carolina de Ferreira, your honesty and realism have kept me grounded and focused.

My heartfelt thanks go to my lab mates, both past and present, who supported me constantly, both inside and outside of the lab: Mitchell Gabalski, Dr. Nate Kauffman, Lucy Xu, Isabelle Lynch, Ece Erder, Dr. Satyendra Singh, and Anastasia Babayan. A special thank you to Chelsea Nayback, for your help on every experiment, no matter how long of a day it was. And especially Dr. Kylie Smith, for all the time dedicated to teaching and guiding me, and for welcoming me into the project that you so lovingly conceived.

And finally, and most sincerely, I want to acknowledge Dr. Kurt Zinn. Thank you for always giving me space to explore and investigate my research questions while always being ready to give advice or recommendations when I found I needed them. Thank you for creating an environment of genuine collaboration and comradery and for welcoming me into that space. Thank you for encouraging me to believe in myself and helping me to become the scientist I am today.

Each of you has played an integral part in this journey, and I am profoundly grateful for your support, guidance, and friendship. From the bottom of my heart, thank you.

PREFACE

My time in Dr. Kurt Zinn's lab has surprised me in many ways. I joined the lab in 2022, knowing I would be exposing myself to numerous new things. I was incredibly lucky to have stumbled into a group of brilliant, kind, and encouraging scientists who made my two years in the lab an incredible journey of growth.

Despite a background rooted in genetics and clinical veterinary medicine, I was assigned to a neuroimaging-focused project. I was chosen for this project because of my passion for working with animals and my desire to develop new surgical techniques. My background provided a solid foundation but did not prepare me completely for the unique challenges and discoveries that lay ahead. This opportunity has allowed me to learn and grow in ways I did not anticipate.

Throughout my years in the Zinn lab, I faced many moments of self-doubt and often did not feel confident in my abilities as a researcher. However, the unwavering support and encouragement from my lab mates and Dr. Zinn made all the difference. The lab was a safe space where I could fail, learn from those failures, and continuously improve. Along the way, I surprised myself with my abilities to adapt to new and challenging situations.

I owe a great deal of gratitude to Dr. Zinn for his mentorship, patience, and belief in my potential. His guidance has been instrumental in my growth as a researcher.

I also extend my heartfelt thanks to you, the reader, for taking the time to engage with my work. Thank you for joining me on this journey.

Sincerely,

Katherine M Brown

East Lansing, MI, June 18th, 2024

TABLE OF CONTENTS

LIST OF ABBREVIATIONS

^{18}F-FDG	2-deoxy-2-[^{18}F]fluoro-D-glucose
^{18}F-FDS	2-deoxy-2-[^{18}F]fluorosorbitol
Aβ	Beta-amyloid protein
aCSF	Artificial cerebrospinal fluid
AD	Alzheimer's Disease
AQP4	Aquaporin-4
BBB	Blood brain barrier
CE-MRI	Contrast-enhanced magnetic resonance imaging
CNS	Central nervous system
CPM	Counts per minute
CSF	Cerebrospinal fluid
DAD	Diode array dector
DDM	Dodecyl maltoside
FOV	Field of view
GBCA	Gadolinium-based contrast agent(s)
GS	Glymphatic system
H_2O	Water
HCl	Hydrochloric acid
HILIC	Hydrophilic interaction chromatography
HPLC	High performance liquid chromatography
HT	High-throughput
ICM	Intra cisterna magna
IP	Intraperitoneal
IT	IT
IV	Intravenous
MeCN	Acetonitrile
MIP	Maximum intensity projection
MR(I)	Magnetic resonance (imaging)
N2B	Nose-to-brain
$NaBH_4$	Sodium borohydride

NaOH	Sodium hydroxide
NFT	Neurofibrillary tangle
NIA	National Institute on Aging
NMR	Nuclear magnetic resonance
NREM	Nonrapid eye movement
PET	Positron emission tomography
RadioTLC	Radiation-sensitive thin layer chromatography
RF	Radiofrequency
RPM	Rotations per minute
SAS	Sub-arachnoid space
TAC	Time activity curve(s)
TDM	Tetradecyl maltoside
TFA	Trifluoroacetic acid
TTP	Time to peak (activity)
UV	Ultraviolet
VOI	Volume(s) of interest

1. LITERATURE REVIEW AND INTRODUCTION

1.1. Background

1.2.1 Alzheimer's Disease

More than 50 million people have been diagnosed with Alzheimer's Disease (AD), worldwide. AD patients typically present with dementia, progressive memory loss, and impairments to speech, perception, and motor skills. No cure for AD exists, meaning many patients live with this disease for years. With the number of AD patients expected to double every 5 years, AD presents an enormous burden on the patient, their familites, and the economy, globally estimated at $1 trillion annually[1].

The pathophysiology of AD includes the accumulation of extracellular beta-amyloid (Aβ) deposits and neurofibrillary tangles (NFTs), which begin intracellularly, but become extracellular as the neuron housing the NTFs die. In early AD, the accumulation of Aβ deposits and NFTs promote synaptic loss in the neocortex and the limbic system, causing memory loss. In later stages, the severe acumulation of these proteins leads to severe impairments in cognition and function. Late-stage functional deficits often include difficulties swallowing and urinating, complications that eventually result in the patient's death[1].

AD can be diagnosed using a combination of different assessments. These tests may include neurological examinations, functional assessments, patient and family interviews, analysis of proteins present in cerebrospinal fluid (CSF), and medical imaging such as magnetic resonance imaging (MRI) or positron emission tomography (PET). In this context, PET/MR images are used to exclude other diagnoses in order to support the diagnosis, but they are not the main diagnostic criteria[1, 2].

MRI can be used to assess structural losses in AD patients. In mild AD, hippocampal atrophy occurs at a rate of apprixumately 3-5% per year. Often, by the time that patients are imaged, hippocampal volumes are already reduced by approximately 15-25%, indicating that disease progression has been underway for a number of years. Even in longitudinal studies of patients who were initially asymptomatic, but eventually developed clinical AD, multi-disciplinary clinical diagnoses were made when whole brain volume was decreased by about 6%. Additionally, while MRI is valuable for detecting structural changes, it lacks molecular specificity. It cannot directly identify the presence of Aβ plaques

or NFTs. PET imaging with appropriate tracers can detect Aβ plaques and can be useful for determining more specific causes of dementia, as described in a later section.

In 2012, the unique interstitial fluid exchange system in the brain was identified and named the glymphatic system (GS)[3]. The discovery of this waste clearance system and its subsequent implication in disease pathologies, including AD, opened new avenues for study.

1.2.2 The Blood Brain Barrier

The blood brain barrier (BBB), a feature found in all vertebrates, is a highly selective barrier that exists between the CNS and all surrounding blood vessels. The protection afforded to the brain by the BBB disallows the waste clearance mechanism seen in the lymphatic system from occurring within the CNS[4]. The BBB is a product of tight endothelial junctions made from the walls of the blood vessels that run adjacent to or penetrate the CNS. The endfeet of astrocytes enforce these tight endothelial junctions by wrapping themselves around vessels[4, 5]. Large molecules and hydrophilic substances cannot cross the BBB without being transported, either via transporters or endocytosis. Small lipophilic molecules, however, can diffuse freely across the BBB[5, 6].

The primary function of the BBB is to protect the brain from harm by maintaining homeostasis within the CNS[6, 7]. Dysfunction of the BBB is known to be associated with diseases such as stroke, multiple sclerosis, and AD[5]. The selectivity of the BBB prevents most drugs and imaging agents from being delivered systemically through standard oral or intravenous routes[7, 8]. To bypass the BBB, a drug or agent may be directly injected into the CNS via manual injection[6, 7, 9]. Manual intrathecal (IT) injection, however, is invasive and impractical for repeated administration of a drug[6, 7]. Some research animal models can be obtained with a surgically implanted intracisternal magna (ICM) cannula, allowing for direct access to the sub-arachnoid space (SAS). Some drugs can also be delivered to the brain intranasally via the nose-to-brain (N2B) pathway[7, 8].

1.2.3 N2B Drug Delivery

Delivery of a drug to the central nervous system through the N2B pathway requires the drug to traverse the nasal epithelial structures, the nasal mucosa, and to further diffuse throughout the CNS. This process begins when the drug is introduced to the nasal cavity. The nasal cavity is the cavity that extends from the nostrils to the nasopharynx in

mammals. This passage contains four different types of epithelia, two of which are innervated with cranial nerves: the olfactory epithelium and the respiratory epithelium[6].

The olfactory epithelium is responsible for perception of smell and is innervated by olfactory sensory neurons. These dendritic process of these bipolar cells extends into the mucus layer that coats the surface of the epithelium[6]. The axons of the olfactory sensory neurons penetrate the basal lamina of the epithelium and aggregate to form sheathed nerve bundles that comprise the olfactory nerve (Cranial Nerve I)[6]. The olfactory nerve penetrates the cribriform plate to reach the olfactory bulb[6].

The respiratory epithelium functions to produce mucus and nasal secretions and to propel those secretions to the nasopharynx. This epithelium is innervated with the trigeminal nerve (Cranial Nerve V)[6]. Fibers of the trigeminal nerve extend most of the way through the epithelium; their free nerve endings can be found at the same depth as the tight junctions of adjacent epithelial cells[6]. Most branches of the trigeminal nerve project to the pons, but some also interface with the olfactory bulb[6].

For a drug to enter the CNS with the N2B pathway, it must first be transported across the olfactory or respiratory epithelia, either intracellularly or extracellularly (Figure 1). Large molecules may be transported via endocytosis followed by intraneuronal transport or via transcytosis[6]. Extracellular transport relies on diffusion down the nerves that penetrate the epithelial layer. It is believed that this diffusion occurs within the perineural space[6]. The tightness of the tight junctions between epithelial cells is not yet well understood, but studies have shown that this tightness can be modulated to enhance N2B absorption by compounds such as dodecyl maltoside (DDM) and tetradecyl maltoside (TDM)[10, 11]. Extracellular diffusion past the basal surface of the epithelial layer and into the lamina propria allows a drug to take one of three paths: absorption into systemic blood circulation, absorption into lymphatic vessels, or diffusion into deeper CNS structures[6]. Absorption into systemic blood circulation renews the requirement for consideration of how a drug interacts with the BBB before considering whether the drug will enter the CNS. Entry of a compound directly into deeper CNS structures from the lamina propria is facilitated by diffusion into compartments adjacent to the cranial nerves, including

perineural and perivascular spaces[6].

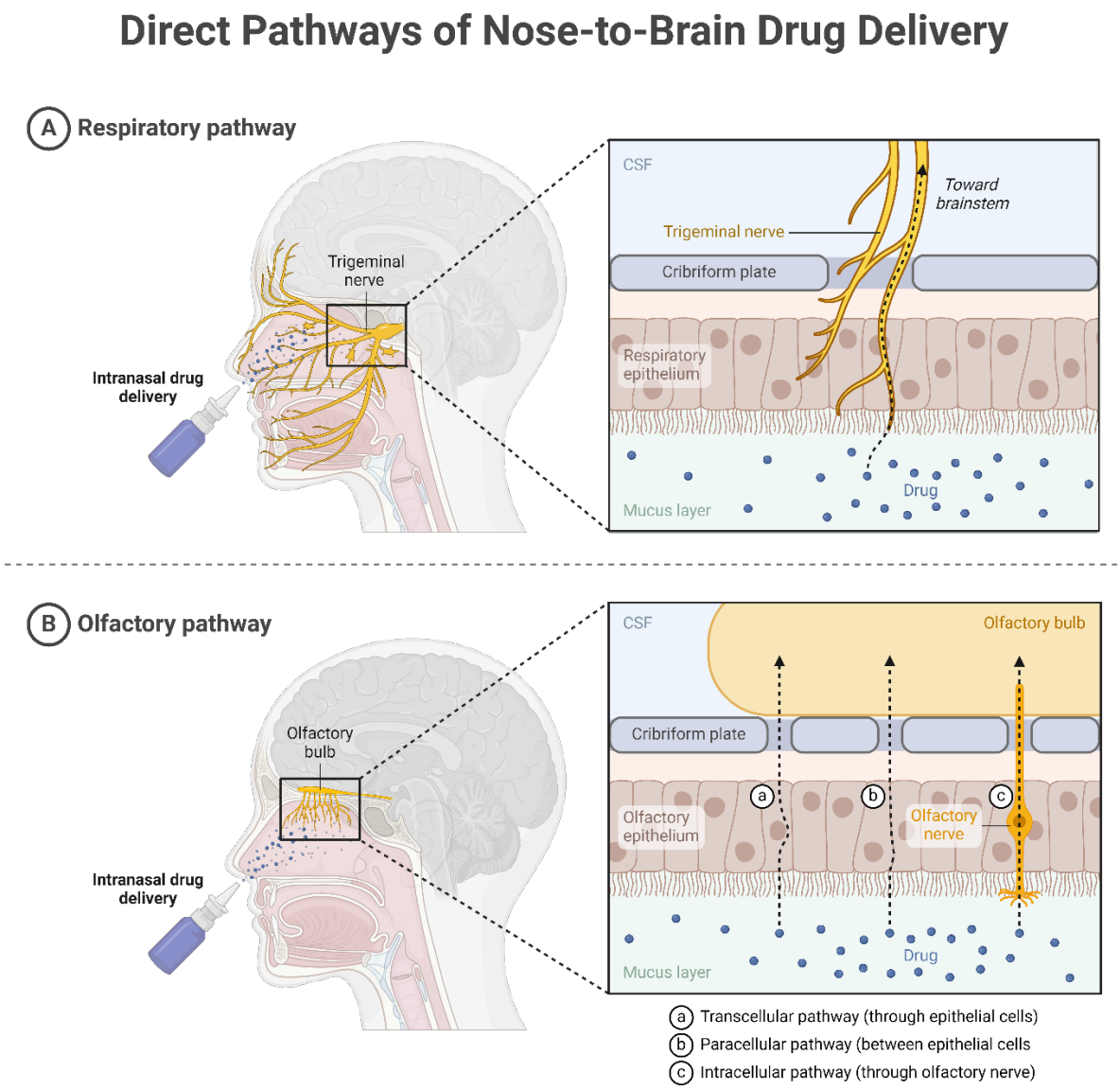

Figure 1: Direct pathways of nose-to-brain drug delivery. Diagram showing both the respiratory and olifacotry pathways. In Panel A, the drug crosses the respiratory epithelium and reaches the brain via the trigeminal nerve. Panel B depicts the olfactory pathway, with the drug traversing the olfactory epithelium and entering the brain via the olfactory nerve.

1.2.4 Lymphatic versus Glymphatic Clearance

Outside of the CNS, the lymphatic system is responsible for waste clearance (Figure 2). In peripheral tissues, arterial capillaries are porous, allowing for blood plasma to exit the vessel and perfuse through the interstitial space of the tissue before entering the lymphatic

capillary bed. From the capillary bed, lymph enters lymphatic vessels through permeable endothelial cell junctions[4, 12]. These junctions are discontinuous and referred to as 'button-like', since they allow fluid and some larger molecules to enter the lymphatic vessel through one-way valves, which prevent backflow[12]. As plasma ultrafiltrate moves through the interstitial space, it picks up waste and globular proteins, eventually carrying those molecules out of the interstitial space through lymphatic capillaries. From the lymphatic capillaries, the fluid, called lymph, and the waste products travel through collecting ducts before reaching lymph nodes[4, 13]. The forward flow of lymph results from the contractile action of smooth muscles, skeletal muscles, and blood vessels[12].

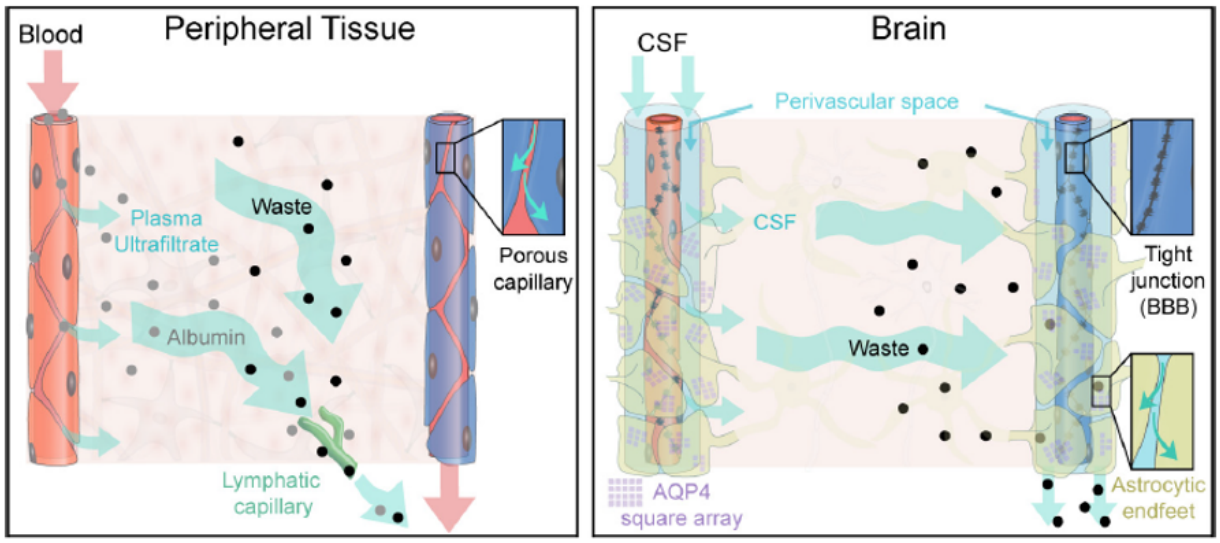

Figure 2: Comparison of waste clearance in peripheral tissues versus the brain. Figure depicting the anatomical and physiological differences in waste clearance in peripheral tissues versus the brain. Figure 1 from Rasmussen, M.K., Mestre, H. & Nedergaard, M. Fluid transport in the brain. Physiological reviews 102, 1025-1151 (2022).

Because the BBB prevents the use of blood plasma as extracellular fluid, the brain utilizes cerebrospinal fluid (CSF) as its primary circulating extracellular fluid[4]. The density of the cerebrospinal fluid is similar to that of the cellular matter of the brain and the spinal cord, allowing the suspension of the brain and spinal cord within the bony cavity of the skull and the spinal cord[4]. The mechanism of CSF secretion is not completely understood, but it is thought that approximately 80% of CSF is produced by the choroid plexus tissue within the third and fourth ventricles of the brain. The remaining 20% of CSF is thought to be produced by the BBB and the parenchymal tissues of the brain[4, 14].

The astrocytic endfeet that help to enforce the BBB do not wrap directly around the blood vessels. The space that exists between the blood vessels and the astrocytic endfeet is called the perivascular space or the Virchow-Robin space[4, 15]. The anterograde flow of CSF is partially driven by the peristaltic action of arterial pulsation[4, 16]. Flow of CSF is also driven by the continued production of CSF. Because the CNS is contained within the bony cavity of the skull and spinal cord, the production of new CSF forces intracranial fluid to drain into peripheral tissues[4]. In a healthy individual, the astrocytic endfeet that form the outer wall of the perivascular space are rich with aquaporin-4 (AQP4) water channels, facilitating the movement of CSF out of the perivascular space and into the parenchyma of the brain. As CSF moves through the interstitial space of the parenchymal cells of the brain, it washes out waste products and toxic proteins such as Aβ, tau, and α-synuclein, a characteristic pathology of Parkinson's disease[3, 17-22].This waste removal primarily occurs during the nonrapid eye movement (NREM) portion of sleep as interstitial space in the brain increases by 60% during sleep or anesthesia[23, 24].

Deviations from normal glymphatic function can result in age-related changes to cognition or severe disease. As individuals age, there is an increased likelihood that astrocytes will mislocalize AQP4 channels, decreasing the number of channels located on the endfeet of the cell[20]. Studies have shown that the loss of polarized AQP4 expression greatly reduces CSF infiltration. This leads to decreased CSF movement through the parenchymal tissue of the brain, decreasing the waste removal power of the glymphatic system[4, 20, 21]. One study found that the deletion of *Aqp4* reduces the bulk flow of CSF by approximately 70% and clearance of exogenous Aβ by approximately 55% in mice[3].

1.2.5 Animal models

Unfortunately, many of the pathologies associated with neurodegenerative diseases and cognitive decline in humans are not naturally seen in animals. Rodents are commonly used to study aging, but they do not naturally display protein misfolding pathologies such as the accumulation of amyloid plaques nor tau-based neurofibrillary tangles[25]. Lines of transgenic mice that accumulate such protein aggregations have been made, transgenic rats still lack accumulation of neurofibrillary tangles. Many factors must be included when considering what constitutes a "good" model of AD is still hotly debated[25]. Aging and age-related disease research relies heavily on the use of rodent models due to their low cost,

ease of genetic and environmental manipulation, and short lifespan[26]. The National Institute on Aging (NIA) even maintains multiple colonies of strains recommended for aging research, including a Fischer F344 line, a Brown-Norway line, and an F1 hybrid of the two[26].

1.2.6 Magnetic Resonance Imaging

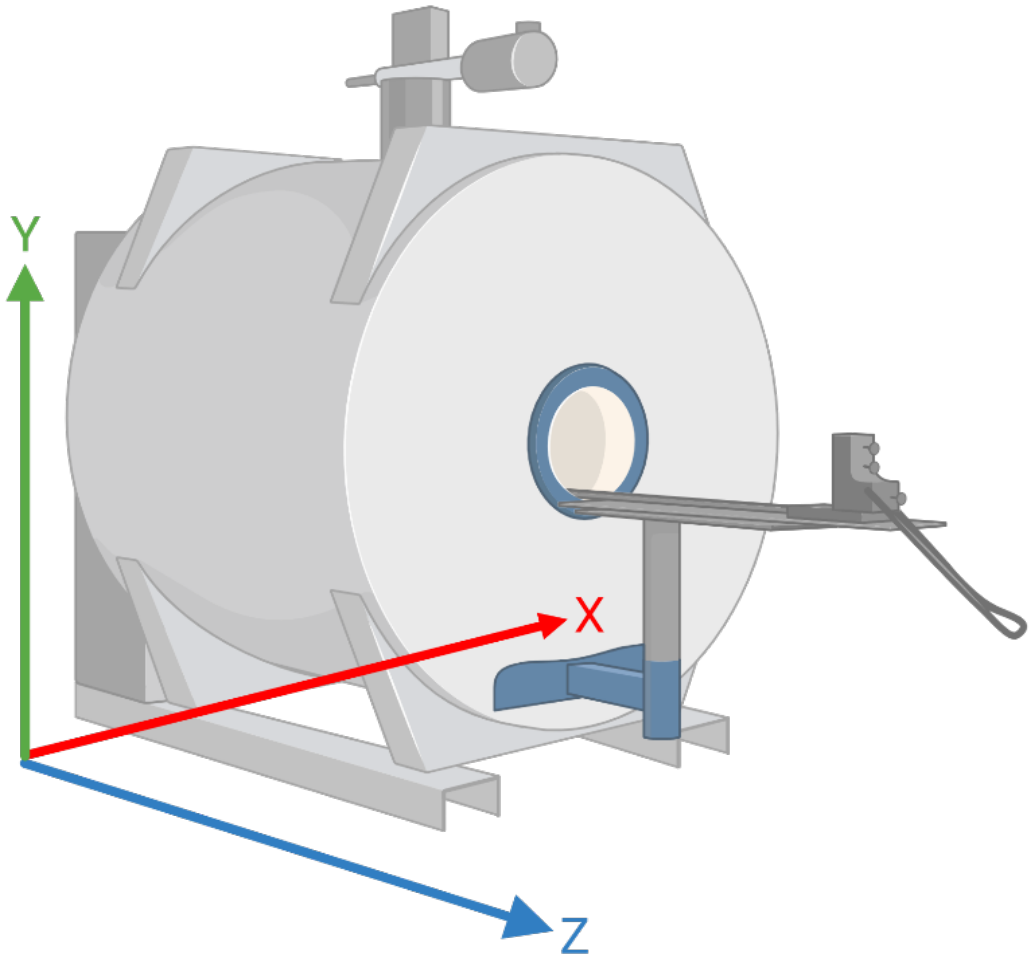

Figure 3: MRI scanner plane directions. An image depicting the standard directions used when discussing the physics of MRI. When using a three-dimensional coordinate system to describe direction relative to an MRI scanner, the Z-axis describes depth, the Y-axis describes height, and the X-axis describes width.

Our understanding of glymphatic structure and flow is due largely to the use of magnetic resonance imaging (MRI)[9]. MRI relies on the principles of nuclear magnetic resonance (NMR) to generate images. Using a three-dimensional coordinate system to

describe direction relative to an MRI scanner, the Z-axis describes its depth (looking into the bore of the MRI), while the Y-axis describes its height, and the X-axis describes its width (**Error! Reference source not found.**). If a large enough static magnetic force is applied in the Z direction, the spin of all hydrogen atoms within the magnetic field will align with that force. The atoms will precess around the vector of the applied magnetic force at a characteristic frequency, known as the Lamor frequency, determined by the gyromagnetic ratio of the atom and the strength of the magnetic field. While the hydrogens all precess at the same frequency, they do not do so in sync with each other. The lack of precessional phase creates a net zero force in the X-Y (transverse) direction, resulting in a main magnetic vector also in the Z direction, matching the static magnetic force. However, the precession of the hydrogen atoms can be synced by applying a radiofrequency (RF) pulse at the frequency of the precession of the hydrogen atoms. When the matching RF pulse is applied, the hydrogen atoms precess in phase and at a wider angle around the Z axis and start gaining magnetization in the transverse direction. This phenomenon, called resonance, generates a rotating transverse magnetic force whose strength is proportional to the length of application of the RF pulse. The rotating magnetic force generates an electrical signal within the RF coil of the MRI. This signal is the basis of how MR images are constructed. When the RF pulse stops, two independent processes occur simultaneously which cause the loss of transverse magnetization and the regaining of longitudinal magnetization. Transverse decay, also known as spin-spin relaxation or T2 relaxation, describes the process where transverse magnetization is lost through the dephasing of the precessing hydrogens. This occurs more rapidly in denser tissues as the hydrogens are more likely to interact and knock each other out of phase. Longitudinal recovery, also known as spin-lattice relaxation or T1 relaxation, describes the process by which the precessing hydrogens regain magnetization in the longitudinal direction. This also occurs more rapidly in denser tissues, as atoms with spin – like hydrogen – are more likely to interact with atoms or molecules without spin in a way that encourages the hydrogens to realign with the static magnetic field in the Z direction. If the appropriate sequence is used, the differing rates of relaxation between tissues generate contrast. The use of different imaging sequences allows for the differentiation of anatomy within a scan[27].

The differentiation between tissues can be made even more stark with the

administration of a paramagnetic contrast agent. Gadolinium-based contrast agents (GBCA), the most commonly used class of paramagnetic contrast agents, greatly decrease T1 relaxation time by encouraging spin-lattice interactions which encourage longitudinal recovery in a type of imaging referred to as contrast-enhanced MRI (CE-MRI)[27]. CNS imaging following GBCA administration is commonly used for research and medical diagnoses, including identification of inflammatory and neurovascular diseases[28].

MRI machines are widely available for research and clinical use[29]. In clinical practice, MRI images are primarily for qualitative comparisons. Using MRI to generate quantitative data in the clinical setting is generally limited to measuring the size of anatomical structures[30]. MRI quantification is limited by the time required to generate the data necessary for quantification. A minimum of two images are required to quantitatively map the properties of tissues, and each image takes multiple minutes to acquire. This limits the use of quantification to only those pathologies that are relatively stable and unchanging over time. Secondly, and most importantly, MRI lacks reproducibility. Even on the same scanner, changing the scanning sequence by as little as a few milliseconds can drastically change the appearance and contrast of tissues[30]. This issue is compounded further when one considers that there are multiple companies that manufacture MRI scanners with unique softwares for interfacing with each different brand of scanner[30]. Those who manufacture the MRI scanners commonly optimize these scanning sequences and publish their recommended sequences for each common type of scan[30]. Studies have highlighted the appreciable differences between images collected from the same tissue imaged with different scanners using the recommended sequences[30]. Because of these issues, the MRI can be considered semi-quantitative, especially when compared to positron-emission tomography (PET).

1.2.7 Positron Emission Tomography

PET is quantitative by nature. PET relies on the positron emission of a radiotracer to provide a signal. All radioisotopes suited for PET undergo β^+ decay, where a proton in the nucleus of the radioisotope converts to a neutron after it releases a positron. PET signal is derived from the collision of the released positron with a free electron within a few millimeters of the decay event. Because the positron is the electron's antiparticle, their collision results in the annihilation of both particles and the release of two gamma ray

photons. These gamma ray photons always have an energy of 511 keV and travel in opposite directions, exactly 180° apart. When the detector array of the PET scanner observes two signals within a short time interval, termed the coincidence interval, the scanner assumes that these signals both originated from the same annihilation event. The line between the two detectors which observed the signals called the line of response and is assumed to contain the annihilation event. Using these observations, PET images show the localization of these annihilation events and the density of their occurrences. This is quantitatively derived from the mathematical determination of the exact position of each annihilation event through the timed detection of these gamma rays. Knowledge of the decay rate of the radioisotope being used coupled with the PET quantification of the annihilation events allows for the quantification of radioactive activity, and by extension, tracer concentration, in three-dimensional space.

The resolution of PET is fundamentally limited by the distance between the location of emission of the positron and where that positron annihilates with an electron. This distance is dependent on the energy of the emitting isotope but is usually approximately 1-2mm. Higher energy positron emitters, such as ^{15}O will have a poorer resolution than lower energy positron emitters like ^{18}F. This difference can affect the resolution by up to half a millimeter[27].

PET scanners do not recover 100% of the signals created by annihilation events. When annihilation occurs and photons are emitted, some of those photons will be absorbed or scatted by the tissues that they pass through. When the photon interacts with a bound electron, the energy of the photon is sufficient to free the electron from its bond, resulting in an effect called Compton scattering, where the photon is diverted from its original path with less energy than what was present before the collision. If this effect occurs with one or both photons created by an annihilation event, that event will not be properly quantified. These effects are more prominent in denser tissues. Detection errors can also occur through random coincidences in the time of detection. Two uncorrelated photons can be mis-matched and can cause the detection of nonexistent signal. In most of these cases, correction factors can be applied to the reconstruction of the PET scan to largely alleviate this burden.

1.2.8 PET Tracers

Positron-emitting radioisotopes may be chelated to a molecule, allowing for the location and/or the pharmacodynamics of the molecule to be visualized via PET. The application of PET is largely reliant on how the radiolabeled molecule interacts with the body. Radiolabels can be applied to a variety of molecules, including, antibodies, amino acids, antigens, sugars, or even water[31]. Most commonly, ^{18}F is chelated to a 2-deoxyglucose, a glucose analog, to create 2-deoxy-2-[^{18}F]fluoro-D-glucose (^{18}F-FDG) and used to detect cancerous tissues with abnormally high glucose consumption throughout the body. When the ^{18}F-FDG is metabolized by the abnormal tissue, the ^{18}F is retained and can be visualized by PET[31].

Fluorine is the single most electronegative element. This allows the formation of exceptionally strong bonds which are usually metabolically stable, making radiofluorinated compounds extremely desirable as radiotracers[32]. ^{18}F naturally occurs at trace levels and can be industrially produced using a cyclotron. In this environment, ^{18}O can be bombarded with high energy protons to create ^{18}F, which can then be chemically substituted onto a desired molecule[32]. Due to the popularity of its use in medicine, ^{18}F distribution systems exist around the world to increase access to ^{18}F-labeled pharmaceuticals[27]. ^{18}F has a radioactive half-life of 109.77 minutes. It may undergo two types of radioactive decay; however, one is much more prominent than the other. ^{18}F decays to ^{18}O via β^+ decay approximately 97% of the time or via electron capture approximately 3% of the time[32].

1.2.9 Use of PET for Detection of Disease

PET imaging has been used in the clinical detection of dementia and AD, with uses dependent on the tracer being used. The results of ^{18}F-FDG PET imaging may help to distinguish between diagnoses for patients with a recent history of cognitive decline who meet the diagnostic critera for both AD and dementia[33]. PET imaging following administration of ^{18}F-FDG is used to assess brain metabolism, which is decreased in the brains of AD patients[34]. Aβ plaques have been detected using administration of radioisotope-bound antibodies and subsequent PET imaging in a procedure known as Amyloid PET[35].

1.2.10 High Performance Liquid Chromatography

High performance liquid chromatography (HPLC) is an extremely sensitive method for

detection of compounds within a sample and the concentration of those compounds and is commonly used for the separations and indetification of sugars[36]. HPLC systems separate compounds within a sample based on their chemical properties. The system utilizes a column containing a stationary phase and a liquid mobile phase solvent with opposite chemical properties. Most commonly, the polarities of the mobile phase and stationary phase contrast. To promote separation of chemicals within a sample, the stationary phase chosen should be similar to the compounds of interest[36]. When a small amount of liquid sample is injected into the HPLC circuit, the sample reaches the column containing the stationary-phase and is attracted to the column, stopping its motion through the circuit temporarily. The dissimilar mobile phase solvent will continue to flow through the column and will eventually wash each molecule within the sample out at varying times. Once a sample component is washed out of the column, it passes by a detector which records the time taken to wash out the molecule with a peak whose size indicates the amount of molecule present[37].

1.2.11 Purpose of Research

The purpose of this research was to explore the potential of using ^{18}F-FDS as a novel PET tracer for quantitatively evaluating glymphatic clearance in rats. By synthesizing ^{18}F-FDS through a reduction process from ^{18}F-FDG, this study aimed to assess the ability of this method to detect age related changes in glymphatic clearance in rats. Addtitionally, this work evaluated the optimal route for tracer delivery. The goal of this study was to provide a methodology for insight into glymphatic system function and its implications in age-related decline, potentially advancing non-invasive techniques for early detection of neurodegenerative diseases. Both the second and third chapter of this thesis will be submitted for publication.

2. SYNTHESIS OF ^{18}F-FDS

2.1. Introduction

Glucose is metabolized by most tisues, including neurons, erythrocytes, myocytes, and hepatocytes[38]. Sorbitol, on the other hand, is primarily metabolized by the kidneys[39, 40]. Interestingly, certain strains of bacterial cells also metobolize sorbitol[40]. For these reasons, the utility of ^{18}F-FDS is distinct from that of ^{18}F-FDG. ^{18}F-FDS has been used to successfully detect bacterial infections, brain tumors, and inflammation[39, 40]. Because ^{18}F-FDS does not readily cross the BBB, penetration of ^{18}F-FDS into the brain after IV administration has also been used to measure the integrity of the BBB[41].

Due to the desired physiologic effect and the simplicity of chemistry required to reduce ^{18}F-FDG into ^{18}F-FDS, ^{18}F-FDG was the clear choice as the initial compound to be produced for this study. Worldwide distribution networks exist for the clinical use of ^{18}F-FDG[27]; conveniently, one of those distribution sites was Cardinal Health, located on the campus of Michigan State University. Additionally, a facility dedicated to the synthesis and modification of radiopharmaceuticals for research and clinical purposes was available at Michigan State University.

The chemical composition of sorbitol is extremely similar to that of glucose. A simple chemical reduction will open the ring-shaped glucose and turn it into the chain sorbitol (Figure 4). When this reduction is performed on ^{18}F-FDG, 2-deoxy-2-[^{18}F]fluorosorbitol (^{18}F-FDS) is the result[39, 40]. Despite having extremely similar chemical composition, there are marked differences in the ability of cells to metabolize these sugars.

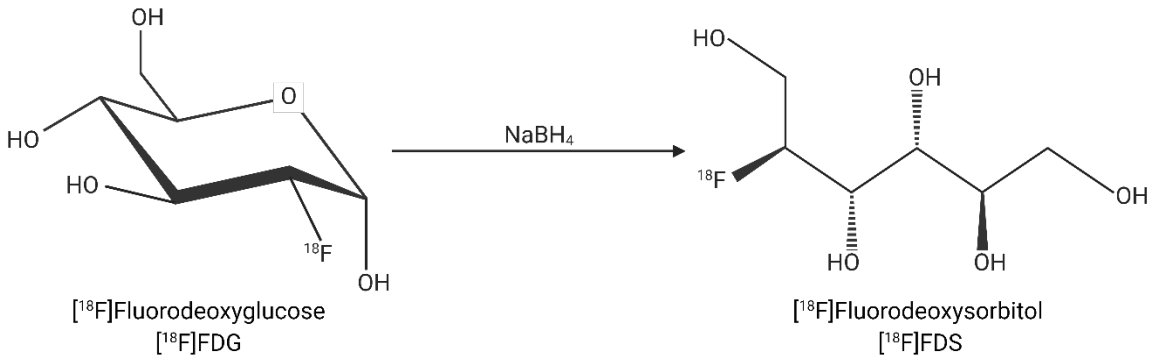

Figure 4: Reduction of ^{18}F-FDG into ^{18}F-FDS. A chemical equation showing the result of reducing ^{18}F-FDG with $NaBH_4$: ^{18}F-FDS.

When choosing a method to assess the effectiveness of the chemical reduction of ^{18}F-FDG into ^{18}F-FDS, access to instrumentation and sensitivity of method were two major considerations. Initially, our group did not have easy access to radioTLC instrumentation, but we did have access to HPLC instrumentation [Agilent 1260 Infinity-II HPLC system equipped with UV-vis and radiation detectors]. HPLC's extreme sensitivity made this method desirable for confirmation of the success of the chemical reduction. This method also allowed for the assessment of purity. The area under the curve (AUC) of each peak corresponds to what percentage that compound is of the whole sample. When equipped with a hydrophilic interaction chromatography (HILIC) column optimized for sugar separation [Phenomenex Luna Omega SUGAR Column], the method was very well suited for the desired purpose. Per previously published literature and manufacturer recommendations, acetonitrile (MeCN) and milliQ H_2O were selected as the mobile phase solvents. The optimized ratio of these was identified through experimentation. A small amount, 0.1% of the total volume, of trifluoroacetic acid (TFA) was later included into the milliQ H_2O component of the mobile phase solvent to stabilize the pH of the combined mobile phase and improve the reproducibility of results.

2.2. Materials and Methods

2.2.1. HPLC Mobile Phase Solvent Optimization

All HPLC modules, including the binary pump [Agilent 1260 Infinity II Binary Pump], diode array dector (DAD) [Agilent 1260 Infinity II Diode Array Detector WR], and radiation detector [Carroll & Ramsey 105-S High-Sensitivity Radiation Detector], were used. Mobile phase solvents of pure MeCN and milliQ H_2O were prepared in separate containers and both connected to the instrument. The machine was primed with both solvents, ensuring that no bubbles were present in the supply lines. The binary pump was set to a rate of 1 mL/min with a ratio of 90:10 of MeCN and H_2O, respecitvely. The pump was allowed to run until the DAD signal was horizontal for more than two minutes, indicating equilibration.

Phamacuetical grade ^{18}F-FDG was obtained from Cardinal Health. Two milligrams of $NaBH_4$ was measured and placed into a 1.5 mL graduated Eppendorf tube and solubilized by adding 2 drops of sterile saline and aggitating. Approxiamtely half of the ^{18}F-FDG stock was transferred into the Eppendorf tube containing the solubilized $NaBH_4$, left open, and placed onto an Eppendorf shaker pre-heated to 37°C at 500 RPM for 10 minutes. After the

reaction had proceeded for 10 minutes, the reaction was quenched with 30 μL of 0.25M HCl, added directly to the reaction tube, and mixed by pipetting up and down.

At least 20 μL of both the ^{18}F-FDG stock and the reaction product were placed into sparate low-volume inserts inside 2 mL HPLC sample vials. Additionally, equal parts of both the ^{18}F-FDG stock and the reaction product were combined in a separate low-volume insert inside a 2 mL HPLC sample vial.

Once the HPLC system reached equilibrium, the ^{18}F-FDG stock, the reaction product, and the mixed sample were assessed under the following run conditions: binary pump rate of 1 mL/min with a a ratio of 90% MeCN to 10% H_2O with no pre-set run stop time; DAD signal wavelength at 210 nm with 4 nm bandwidth, a reference wavelength of 360 nm with a 4 nm bandwidth, and a peak width of 2.5 Hz, using a 2 second response time; and radiation detector probe peakwidth of 6.25 Hz, using a 2 second response time.

On a separate day, this procedure was repeated with a mobile phase solvent ratio of 80% MeCN to 20% H_2O. No other conditions were changed.

2.2.2. Optimization of Reaction Time

Once the desired ratio of MeCN to milliQ H_2O with 0.1% TFA was identified as 80:20, respectively, the minmum reaction time for complete reduction of ^{18}F-FDG to ^{18}F-FDS was assessed with HPLC.

All HPLC modules, including the binary pump, DAD, and radioation detector, were turned on and initialized. Mobile phase solvents of pure MeCN and milliQ H_2O with 0.1% TFA were prepared in separate containers and both connected to the instrument. The machine was primed with both solvents, ensuring that no bubbles were present in the supply lines. The binary pump was set to a rate of 1 mL/min with a ratio of 80:20 of MeCN and H_2O with 0.1% TFA, respecitvely. The pump was allowed to run until the DAD signal was horizontal for more than two minutes, indicating equilibration.

Phamacuetical grade ^{18}F-FDG was obtained from Cardinal Health. A small amount, approximately 20 μL, of ^{18}F-FDG stock was transferred to a low-volume insert inside a 2 mL HPLC sample vial for use as a control sample. The remaining ^{18}F-FDG stock was transfererred to an Eppendorf tube containing 2 mg of $NaBH_4$ solubilized in saline for reduction. The reaction vial was placed, open, onto an Eppendorf shaker pre-heated to 37°C at 500 RPM. After 5 minutes, a small amount of reaction product was removed from

the reaction vial and quenched with 1M HCl. This sample was transferred to a low-volume insert inside a 2 mL HPLC sample vial. This was repeated at 10, 20, and 30 minutes after reaction initiation.

Each sample was assessed under the following run conditions: binary pump flow at 1 mL/min at a ratio of 80 MeCN:20 H_2O with 0.1% TFA and a stop time of 7 minutes; DAD signal wavelength at 210 nm with 4 nm bandwidth, a reference wavelength of 360 nm with a 4 nm bandwidth, and a peak width of 2.5 Hz, using a 2 second response time; and radiation detector probe peakwidth of 6.25 Hz, using a 2 second response time.

2.2.3. <u>Product Stability Study</u>

The stability of the radiochemical reaction product was assessed out to 8 hours using HPLC. All HPLC modules, including the binary pump, DAD, and radioation detector, were turned on and initialized. Mobile phase solvents of pure MeCN and milliQ H_2O were prepared in separate containers and both connected to the instrument. The machine was primed with both solvents, ensuring that no bubbles were present in the supply lines. The binary pump was set to a rate of 1 mL/min with a ratio of 80:20 of MeCN and H_2O with 0.1% TFA, respecitvely. The pump was allowed to run until the DAD signal was horizontal for more than two minutes, indicating equilibration.

Phamacuetical grade ^{18}F-FDG was obtained from Cardinal Health. A small amount, approximately 20 µL, of ^{18}F-FDG stock was transferred to a low-volume insert inside a 2 mL HPLC sample vial for use as a control sample. The remaining ^{18}F-FDG stock was transfererred to an Eppendorf tube containing 2 mg of $NaBH_4$ solubilized in saline for reduction. The reaction vial was placed, open, onto an Eppendorf shaker pre-heated to 37°C at 500 RPM for 10 minutes. The reaction was quenched by adding 53 µL of 1M HCl to the vial and mixing by pipetting up and down. The reaction product was pH balanced by pipetting 2-5 µL of reaction product onto a pH indicator strip and assessing the color as compared to the guide provided on the packaging. The pH was then adjusted using HCl if basic, or NaOH if acidic. The pH was then reassessed using another indicator strip. This was repeated until the pH reached the desired pH of approximately 7.4.

Once pH balanced, a portion of the final reaction product was transferred to a low-volume insert inside a 2 mL HPLC sample vial and kept at room temperature. The sample was assessed 2 hours, 4 hours, 6 hours, and 8 hours after quenching.

2.3. Results

2.3.1. HPLC Mobile Phase Solvent Optimization

The retention times of ^{18}F-FDG and ^{18}F-FDS were analyzed using a radiation detector under different mobile phase solvent ratios. Representative peaks are shown for each condition (Figure 5). When using a mobile phase solvent of 90% MeCN to 10% milliQ H2O, ^{18}F-FDG exhibited a retention time of 8.674 ± 0.011 (n=6) minutes, while ^{18}F-FDS showed a retention time of 12.879 ± 0.028 (n=6) minutes. In contrast, when the mobile phase solvent ratio was adjusted to 80% MeCN to 20% milliQ H_2O, the retention times decreased, with ^{18}F-FDG at 4.153 ± 0.0033 (n=6) minutes and ^{18}F-FDS at 4.998 ± 0.0039 (n=16) minutes (Table 1).

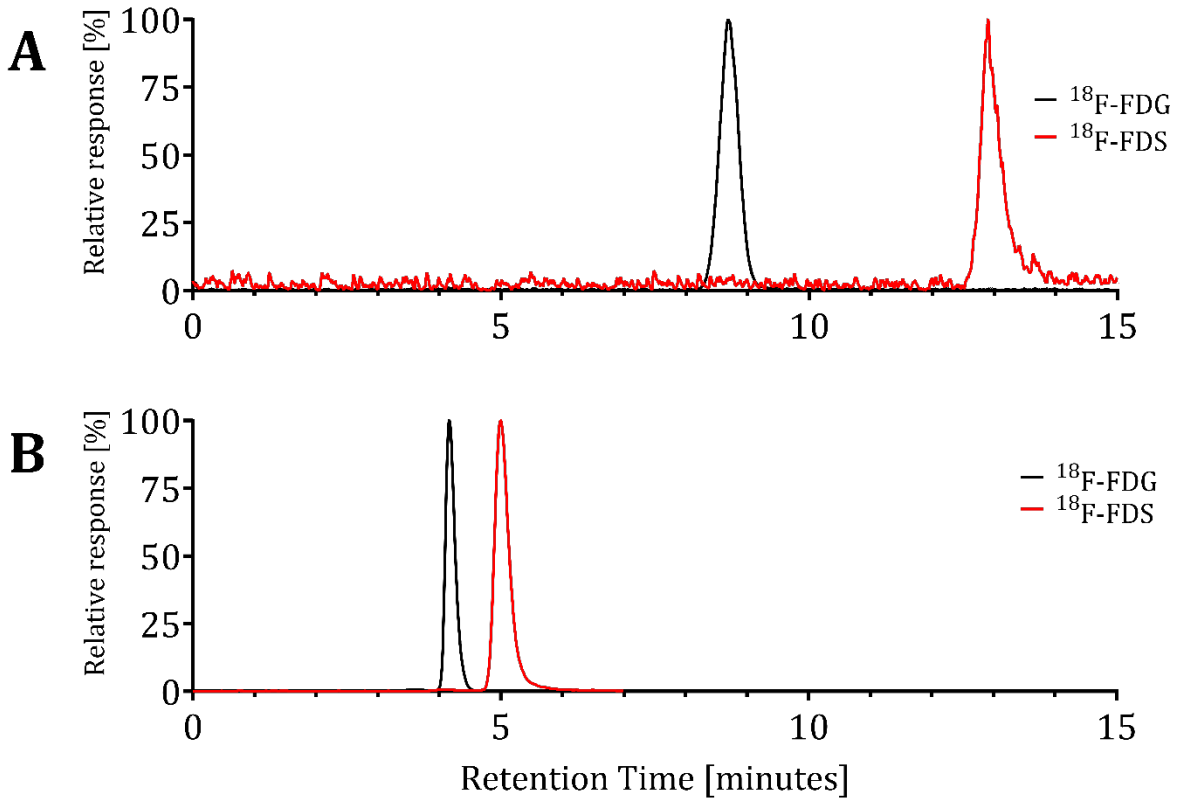

Figure 5: Comparison of HPLC mobile phase solvent ratios. Two graphs are shown, depicting the differences in radiation detector retention times with different mobile phase solvent ratios. (A) shows representative peaks with a 8.69 minute retention time for ^{18}F-FDG and a 12.97 minute retention time for ^{18}F-FDS in a mobile phase solvent of 90% MeCN to 10% milliQ H_2O. (B) shows representative peaks with a 4.17 minute retention time for ^{18}F-FDG and a 5.00 minute retention time for ^{18}F-FDS in a mobile phase solvent of 80% MeCN to 20% milliQ H_2O.

Mobile Phase Solvent Ratio	^{18}F-FDG Retention Time (min ± SE)	^{18}F-FDS Retention Time (min ± SE)
90% MeCN: 10% H_2O	8.674 ± 0.011 (n=6)	12.879 ± 0.028 (n=6)
80% MeCN: 20% H_2O	4.153 ± 0.0033 (n=6)	4.998 ± 0.0039 (n=16)

Table 1: Comparison of HPLC mobile phase solvent ratios. Radiation detector retention times ± standard error are shown for both examined ratios of MeCN to H_2O.

2.3.2. Optimization of Reaction Time

The HPLC retention times associated with no reaction, 5, 10, 20, and 30 minutes of product reaction time were compared. Representative peaks are shown for each condition (Figure 6). The unreacted ^{18}F-FDG exhibited a 4.153 ± 0.0033 (n=6) minute reaction time while all ^{18}F-FDS reaction products exhibited retention times of approximately 5 minutes, regardless of the amount of time allowed for reaction (Table 2).

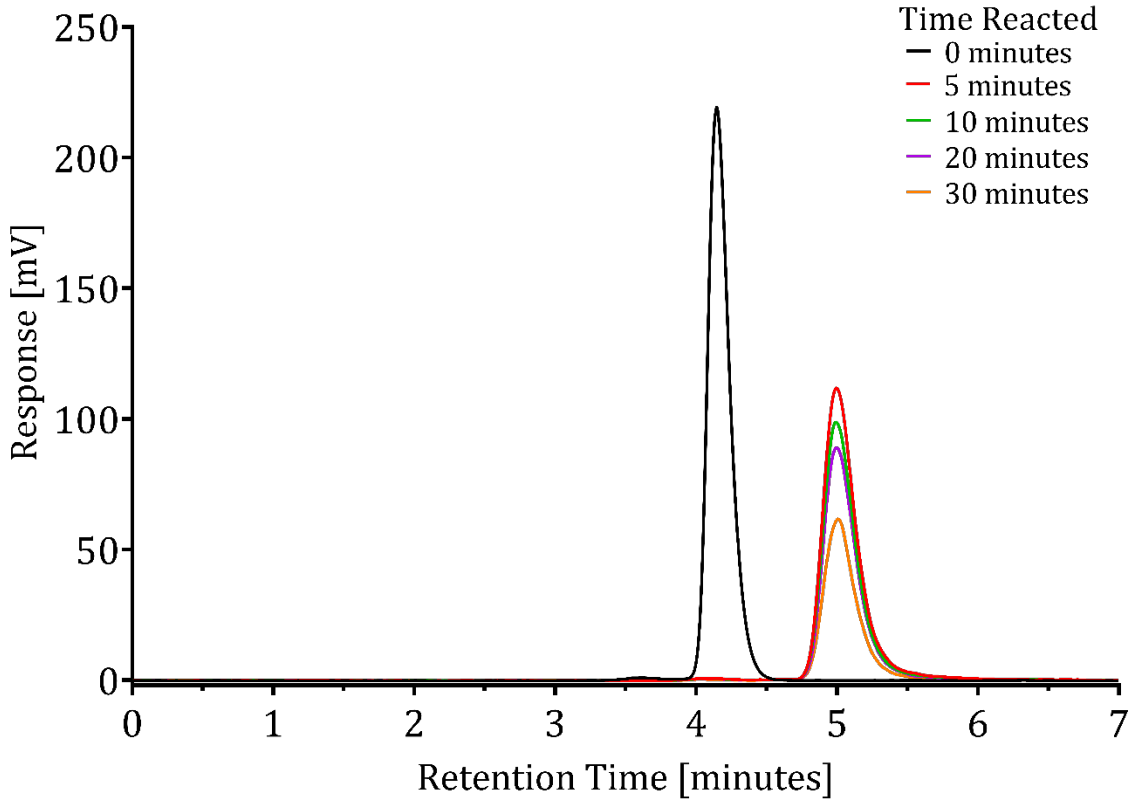

Figure 6: Optimization of reaction time. Plot shows the representative peaks indicating the radiation detector retention times of ^{18}F-FDG as compared to ^{18}F-FDS, as measured after 5, 10, 20, and 30 minutes of reacting before being quenched with HCl to stop the reaction from proceeding further.

Identity	Reaction Time	Retention Time (min ± SE)	Sample Size
^{18}F-FDG	0 minutes	4.153 ± 0.0033	6
^{18}F-FDS	5 minutes	4.9975 ± 0.0015	2
^{18}F-FDS	10 minutes	4.9965 ± 0.0045	2
^{18}F-FDS	20 minutes	5.0027 ± 0.0028	3
^{18}F-FDS	30 minutes	5.0055 ± 0.0035	2

Table 2: Optimization of reaction time. Radiation detector retention times ± standard error is shown for ^{18}F-FDG as compared to ^{18}F-FDS, as measured after 5, 10, 20, and 30 minutes of reacting before being quenched with HCl to stop the reaction from proceeding further.

2.3.3. Product Stability Study

The HPLC retention time of the ^{18}F-FDS reaction product was tested at 2, 4, 6, and 8 hours after the reaction was quenched. Representative peaks are shown for each condition (Figure 7). The unreacted ^{18}F-FDG exhibited a 4.153 ± 0.0033 (n=6) minute reaction time. All ^{18}F-FDS reaction products showed retention times of approximately 5 minutes, with a variation of less than 1% (Table 3). All ^{18}F-FDS reaction product curves were 100% pure.

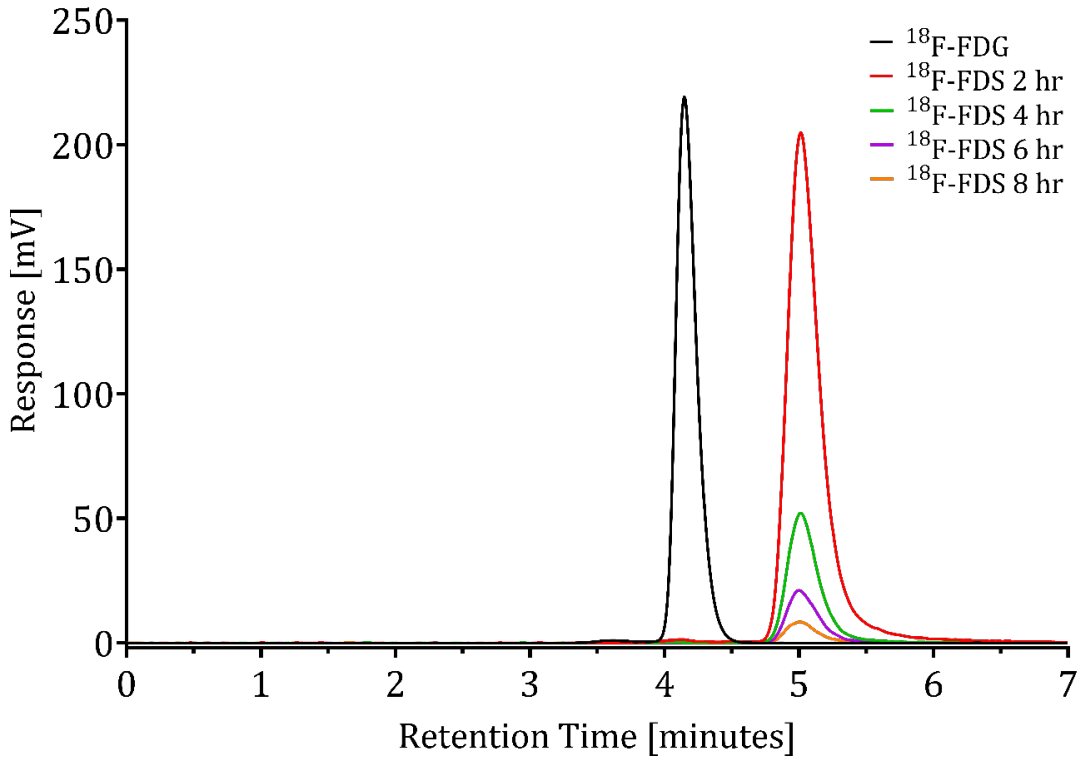

Figure 7: Product Stability Study. Plot shows the radiation detector retention times of unreacted ^{18}F-FDG as compared to ^{18}F-FDS stored at room temperature 2, 4, 6, and 8 hours after reaction.

Identity	Time Post Reaction	% Purity (% AUC ± SE)	Sample Size
^{18}F-FDG	Not reacted	99.56 ± 0.197	6
^{18}F-FDS	2 hours	100 ± 0.0	2
^{18}F-FDS	4 hours	100 ± 0.0	3
^{18}F-FDS	6 hours	100 ± 0.0	2
^{18}F-FDS	8 hours	100 ± 0.0	2

Table 3: Product Stability Study. Radiation detector retention times ± standard error is shown for ^{18}F-FDG as compared to ^{18}F-FDS, as measured 2, 4, 6, and 8 hours after reacting, after being stored at room temperature.

2.4. Discussion

HPLC analysis was used to differentiate between unreacted ^{18}F-FDG and the reaction product, ^{18}F-FDS. This analysis was essential to assess the efficiency of the reaction and the purity of the final product. Because of the vastly different metabolic profiles of the two compounds, successful identification of the reaction product was vital to the success of this work.

During method development, multiple mobile phase solvent ratios were tested. Initially, the HPLC analysis was conducted using a sugar-specific HILIC column with a mobile phase composed of 90% MeCN and 10% H_2O. The flow rate was maintained at 1.0 mL/min, and detection was performed using a radiation detector. Samples of both unreacted ^{18}F-FDG and the reaction product were prepared and injected into the HPLC system for analysis. With this mobile phase solvent ratio, The chromatograms showed distinct and well-resolved peaks for both ^{18}F-FDG and ^{18}F-FDS. The peak at 8.674 ± 0.011 minutes (n=6) corresponded to unreacted ^{18}F-FDG, while the peak at 12.879 ± 0.028 minutes (n=6) corresponded to the reaction product ^{18}F-FDS. The clear separation of these peaks confirmed the successful differentiation between the two compounds, enabling an accurate assessment of the reaction mixture. However, with more than 4 minutes of separation, a more efficient method was desired.

To achieve this, the mobile phase solvent ratio was changed. The HPLC analysis was conducted with a mobile phase composed of 80% MeCN and 20% H_2O with 0.1% TFA. No other conditions were changed. Samples of both unreacted ^{18}F-FDG and the reaction product were prepared and injected into the HPLC system for analysis. The chromatograms

showed distinct and well-resolved peaks for both ^{18}F-FDG and ^{18}F-FDS. The peak at 4.153 ± 0.0033 minutes (n=6) corresponded to unreacted ^{18}F-FDG, while the peak at 4.998 ± 0.0039 minutes (n=16) corresponded to the reaction product ^{18}F-FDS. With these retention times, clear separation of these peaks remained, confirming the successful differentiation between the two compounds, and enabling an accurate assessment of the reaction mixture.

The minimum reaction time necessary to convert ^{18}F-FDG into ^{18}F-FDS was assessed by quenching the reaction with HCl at 5, 10, 20, and 30 minutes after reaction initialization and assessing the products with HPLC. All reaction products showed a complete conversion from ^{18}F-FDG to ^{18}F-FDS as indicated by the retention times and the absence of more than one peak.

The stability of the reaction product was assessed by allowing the reaction product to sit at room temperature and assessing it using HPLC at 2, 4, 6, and 8 hours after the reaction was quenched. All reaction products showed retention times that identified them as ^{18}F-FDS with 100% purity.

The retention times for both ^{18}F-FDG and ^{18}F-FDS were consistent between trials, showing variation of less than 1%. The separation between the peaks was sufficient to ensure that the compounds did not co-elute, which is critical for accurate quantification and assessment of reaction efficiency.

Challenges encountered during the HPLC analysis included slight variations in retention times. The addition of TFA to stabilize the pH of the mixtures assisted in addressing these concerns. Mixing, aggitation, and vacuum filtration of pre-mixed mobile-phase solvent also assisted in reducing variation between trials. The method's limitations include its inability to detect non-chromophoric impurities and potential matrix effects from sample preparation. Future experiments could compare this HPLC-based method to established radioTLC methods.

3. CLEARANCE OF ^{18}F-FDS IN RATS FOLLOWING INTRATHECAL OR INTRANASAL DELIVERY

3.1. Introduction

MRI has been used to charactarize glymphatic clearance since its discovery[9]. It has also has been used in many studies to examine N2B delivery of various agents[4, 42]. Replicable quantification of MR images has long been desired but has not yet been achieved. PET, however, is innately quantitative. This limitation of MR image analysis prompted our hypothesis that PET imaging would be better suited for quantifying glymphatic clearance, compared to MRI.

PET provides sensitive and quantitative data on tracer distribution and activity, making it ideal for tracking the clearance and uptake of ^{18}F-FDS in the brain. However, PET alone lacks the anatomical resolution needed to precisely localize tracer accumulation, but can be complemented by MRI's superior soft-tissue contrast and high-resolution imaging. By combining PET's functional data with MRI's structural imaging, the biodistribution of ^{18}F-FDS could be accurately mapped.

Fisher F344 rats were used because an animal model commonly used for aging studies was desired. Glymphatic clearance is affected by aging, so a model that exhibits age related changes was chosen. This line was originally derived with the intent of use in aging studies by the NIH and has been bred by them and by other suppliers since the inception of the line.

In later experiments, when rats with pre-placed ICM cannulas were acquired, maintaining the strain was desired, but was not possible. For these specialty animals, a more robust strain was recommended by the supplier. This led us to the Sprague Dawley rat strain, a common general purpose rodent model[43].

In this study, the sensitivity of PET imaging to ^{18}F-FDS was evaluated in 8 young sex-balanced Fisher F344 rats compared to 2 aged male Fisher F344 rats. The purpose of this study was to assess the ability of this method to detect age related changes in glymphatic clearance. Subsequently, the biodistribution of ^{18}F-FDS after IT injection was assessed with 3 male middle aged Fisher F344 rats in order to determine the location of tracer accumulation after injection. The effect of absorption enhancers on ^{18}F-FDS N2B uptake was assessed using 6 sex-balanced Fisher F344 rats in order to determine whether

absorption enhancers should be included in dosing formulas for IN experiments. Finally, routes of administration of ^{18}F-FDS were compared using a same-subject design with a total of 6 young female Sprague Dawley rats for the purpose of finding the most efficient route of adminstration of ^{18}F-FDS.

3.2. Materials and Methods

3.2.1. Radiochemistry

Phamacuetical grade ^{18}F-FDG was obtained from Cardinal Health. A few microliters of stock was set asside to be later compared to the reaction product with HPLC or radioTLC. Separately, 0.002 g (2 mg) of $NaBH_4$ was measured and placed into a 1.5 mL graduated Eppendorf tube and solubilized by adding 2 drops of sterile saline and aggitating. The remaining ^{18}F-FDG stock was transferred into the Eppendorf tube containing $NaBH_4$ in sterile saline, left open, and placed onto an Eppendorf shaker pre-heated to 37°C at 500 RPM for 10 minutes. After the reaction had proceeded for 10 minutes, the reaction was quenched with 53 µL of 1M HCl, added directly to the reaction tube, and mixed by pipetting up and down.

The reaction product was pH balanced to the desired pH of approximately 7.4 as previously described. Separately, a Sep-Pak Alumina N Plus Long cartridge was prepared according to manufacturer instructions. Once the desired pH was reached, the reaction product was loaded into the Sep-Pak cartridge. The cartridge was then eluted using 5 mL of sterile saline, creating ten 500 µL fractions in the process. The activity of each fraction was measured and recorded. The fraction with the highest activity was selected for dosing. Finally, the selected fraction was passed through a sterile Whatman 0.2 µm PES Filter into a new Eppendorf tube. A few microliters of the final product was set aside to be later compared to the initial ^{18}F-FDG stock with HPLC (Figure 8). This complete method was repeated immediately prior to each study that required ^{18}F-FDS activity.

3.2.2. HPLC quality control assay

All HPLC modules, including the binary pump, DAD, and radioation detector, were turned on and initialized. Mobile phase solvents of MeCN and milliQ H_2O with 0.1% TFA were prepared in separate containers and both connected to the instrument. The machine was primed with both solvents, ensuring that no bubbles were left in the supply lines. The binary pump was set to a rate of 1 mL/min with a ratio of 80:20 of MeCN and H_2O with

0.1% TFA, respecitvely. The pump was allowed to run until the diade array detector signal was horizontal for more than two minutes, indicating equilibration.

The previously set aside portion of stock sample of ^{18}F-FDG from Cardinal Health was diluted with sterile saline and transferred an HPLC sample vial with low-volume insert. The HPLC vial was transferred to the multisampler tray of the HPLC. The sample was then run using the following analysis method settings: binary pump flow at 1 mL/min at a ratio of 80 MeCN:20 H_2O with 0.1% TFA and a stop time of 7 minutes; DAD signal wavelength at 210 nm with 4 nm bandwidth, a reference wavelength of 360 nm with a 4 nm bandwidth, and a peak width of 2.5 Hz, using a 2 second response time; and radiation detector probe peakwidth of 6.25 Hz, using a 2 second response time.

Separately, same procedure was repeated with the previously set aside portion of the reaction product.

The retention times of the two samples were compared to each other and to known values obtained under the same conditions for assessment of complete reduction of ^{18}F-FDG to ^{18}F-FDS. This assessment method was utilized prior to each study that required ^{18}F-FDS activity.

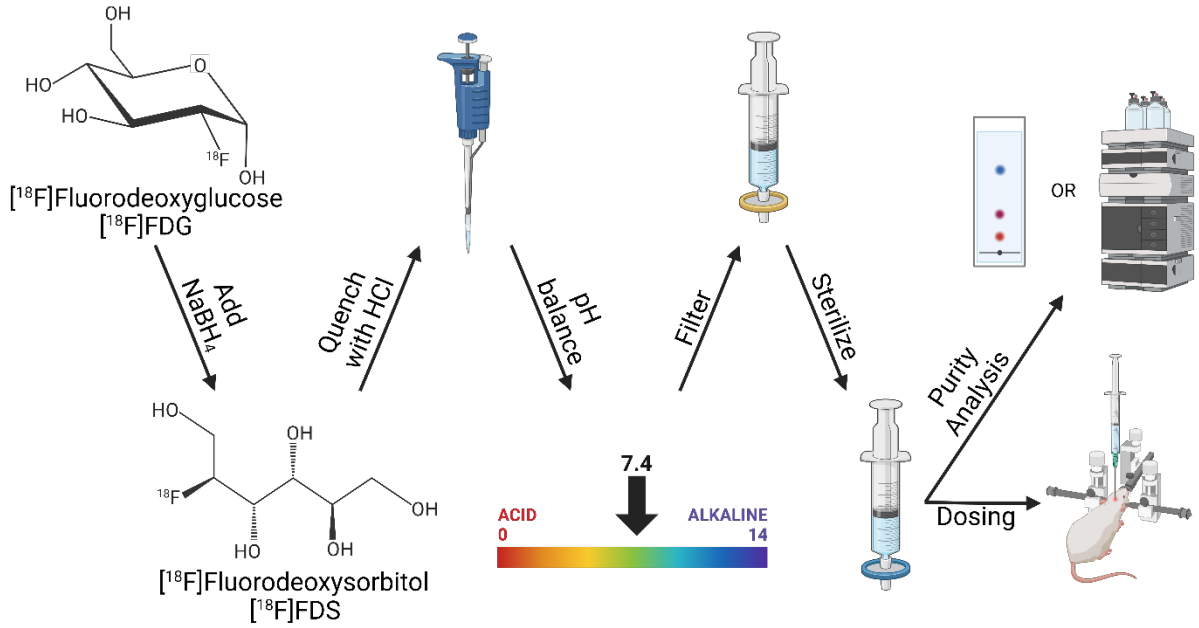

Figure 8: Radiochemistry Methods. The figure illustrates the stepwise process involved in the conversion of ^{18}F-FDG into ^{18}F-FDS. The process began with chemical reduction, followed by reaction quenching, then pH balancing before filtration and sterilization of the dose. A small portion of the final dose was analyzed while the rest was administered.

3.2.3. IT administration of ^{18}F-FDS in young animals

Brain activity following IT administration of ^{18}F-FDS was tested in young (6-month-old) Fisher F344/NHsd rats (n=8, sex balanced). Before injection, each animals' hair was removed along the dorsal surface from the crown of the skull to the beginning of shoulder using clippers and Nair. Animals were anesthetized with isoflurane. The animal's eyes were lubricated, and each animal was brought to a baseline level of hydration with an intraperitoneal (IP) injection of 2 mL of sterile saline. Once the animal was at an appropriate anesthetic depth, they were transferred to a stereotaxic frame. Using the positioning controls of the frame, the animal was positioned with the nose tilted down, exposing the base of the skull and the cisterna cerebellomedullaris cavity. The shaved area was sterilized using 70% alcohol wipes and iodine swabs.

A syringe pump was loaded with a syringe connected to a long catheter, comprised of a 30G needle tip set bevel out into PE-10 tubing, with a 30G needle and hub set bevel in into the opposing end. Using the syringe pump, the dose was withdrawn into the catheter so that there was no air at the end, and a drop could be seen in the bevel of the needle. This ensured that no air was injected into the subarachnoid space.

The needle of the catheter was placed into the middle of the cisterna cerebellomedullaris cavity of the animal at a 60° angle to the horizontal axis. The needle was advanced until it had punctured skin, the dura matter, and the arachnoid matter, approximately 8 mm (Figure 9).

Using the multichannel syringe pump, 27 µL of tracer was administered at a rate of 2 µL/min to two subjects simultaneously (Figure 9).. Time post-injection was defined as time elapsed after the beginning of tracer administration. Upon completion of the injection, the needle was kept in place for 2 minutes before being gently removed. After the removal of the needle, animals were kept in position on the frame for an additional 2 minutes.

Animals were subsequently placed in a prone position on a custom 3D-printed high-throughput (HT) bed, allowing for PET/MR imaging of two subjects at once (Figure 9). Each bed was connected to a water circulation system to maintain the animals' body temperature. Respiration and temperature probes were placed to monitor the animals' physiological parameters throughout the scan. The respiration pad was slid under the chest and secured with tape, and the temperature probe was inserted anally. Scans were

executed with continuous monitoring of the animals' physiological parameters.

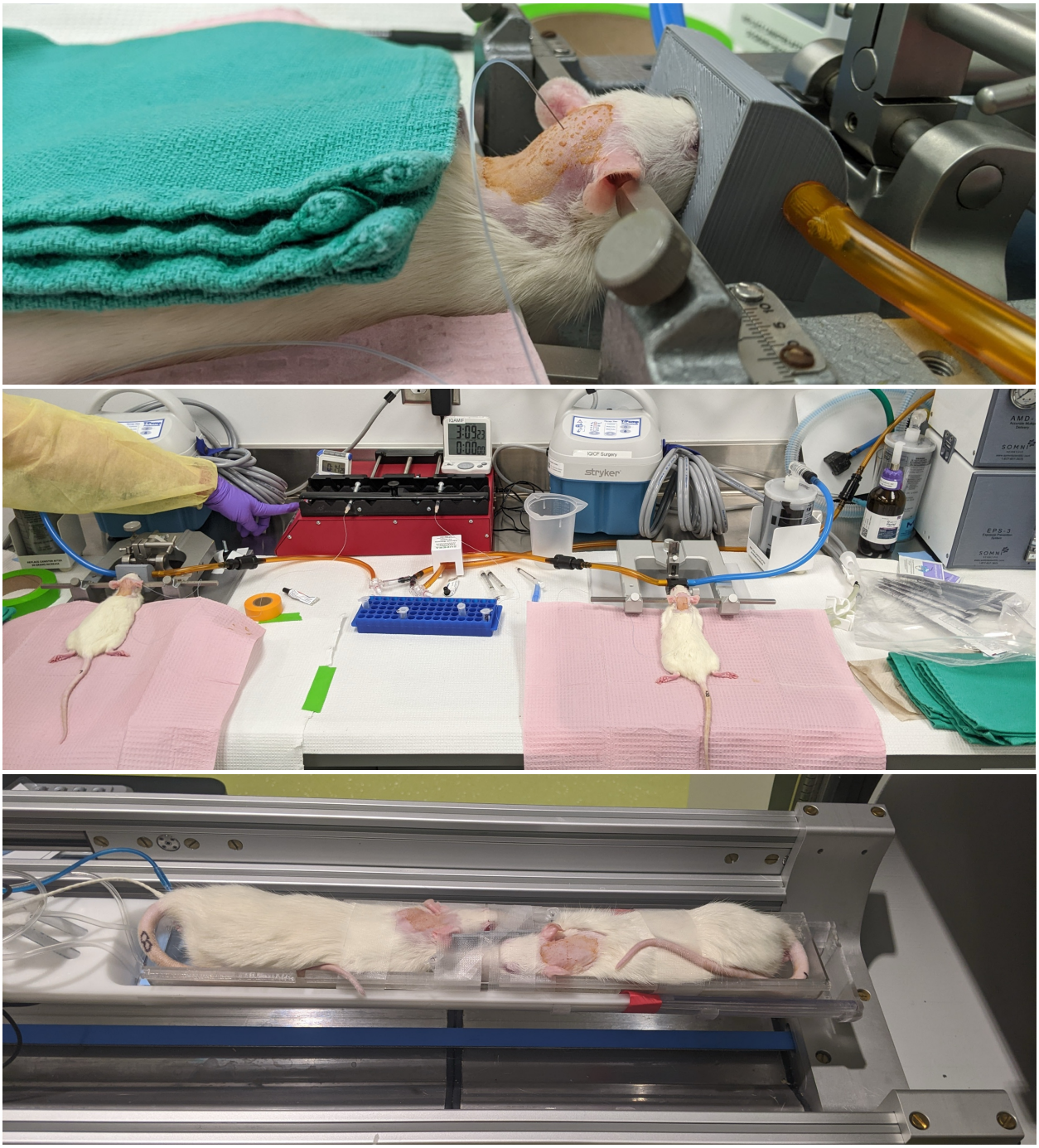

Figure 9: Experiment photographs. Photographs taken during IT administration of ^{18}F-FDS in young animals experiment depicting IT needle placement (top), coadministration of IT ^{18}F-FDS via syringe pump (middle), and post-injection positioning on a HT bed (bottom).

A localizer scan was performed to confirm proper positioning within the field of view (FOV). MRI sequences included T2-weighted Turbo-RARE for anatomical reference. PET

scans were conducted to visualize and quantify ^{18}F-FDS tracer distribution. Simultaneous PET and MR images were acquired at 0.5, 1.75, and 3 hours post injection.

3.2.4. IT administration of ^{18}F-FDS in aged animals

The method used for IT administration in young animals was repeated in aged (27-month-old) Fisher F344/NHsd male rats (n=2). Imaging methods, timepoints, reconstruction method, and analysis methods were maintained from the previous experiment.

3.2.5. Biodistribution of ^{18}F-FDS activity after IT injection

The biodistribution of ^{18}F-FDS one hour after intrathecal injection was assessed in 17-month-old male Fisher F344/NHsd rats (n=3). The previously described IT injection method was used, but animals were not imaged. One hour post-injection, subjects were euthanized using carbon dioxide and subsequent bilateral pneumothorax. Immediately following euthanasia, a thoracotomy was performed to access the heart, and blood was collected via cardiac puncture. Subsequently, major organs and tissues, including the brain, cervical lymph nodes, heart, liver, spleen, kidneys, stomach, intestines, muscle, and bone, were rapidly excised. Each collected tissue sample was placed into pre-weighed gamma-counting tubes. The radioactivity of the samples was measured using a gamma counter calibrated for ^{18}F. The counts per minute (CPM) were recorded for each sample and corrected for background radiation and decay.

3.2.6. IN instillation of ^{18}F-FDS with versus without absorption enhancers

Brain activity after IN instillation of ^{18}F-FDS (n=2, sex balanced) was compared to IN instillation of ^{18}F-FDS with 0.25% w/v DDM (n=2, sex balanced) and ^{18}F-FDS with 0.25% w/v TDM (n=2, sex balanced).

A syringe was fitted with a nasal catheter, consisting of PE-10 tubing with a 30G needle and hub set bevel in into the end opposite the nose. Using the syringe, the dose was withdrawn into the catheter, leaving some air at the end of the catheter.

Animals were anesthetized with isoflurane. The animal's eyes were lubricated, and each animal was brought to a baseline level of hydration with an IP injection of 2 mL of sterile saline. Once the animal was at an appropriate anesthetic depth, the nasal catheter was placed into the left nares and secured with tape. Animals were loaded on a HT bed in the supine position on the HT bed. Physiologic parameter monitoring methods were

maintained from earlier experiments. A localizer scan was performed to confirm proper positioning within the field of view. MRI sequences included T2-weighted Turbo-RARE for anatomical reference. PET scans were conducted to visualize and quantify ^{18}F-FDS tracer distribution.

A sufficiently long catheter was used to allow for dosing to be done while animals were undergoing PET/MR imaging, allowing for alignment of dosing and scan initiation. Dosing was achieved by administering 10 µL every 30 seconds for a total of 50 µL. Subects were imaged dynamically for 10 minutes at 0, 60, and 100 minutes post instillation. Imaging methods, reconstruction method, and analysis methods were maintained from the previous experiment.

3.2.7. Comparison of routes of ^{18}F-FDS administration

3.2.7.1. IT Condition

Using young (4-month-old) female Sprague-Dawley rats with surgically implanted IT cannulas, three different routes of ^{18}F-FDS administration were compared: IT (n=2) , IN (n=2), and IV (n=6).

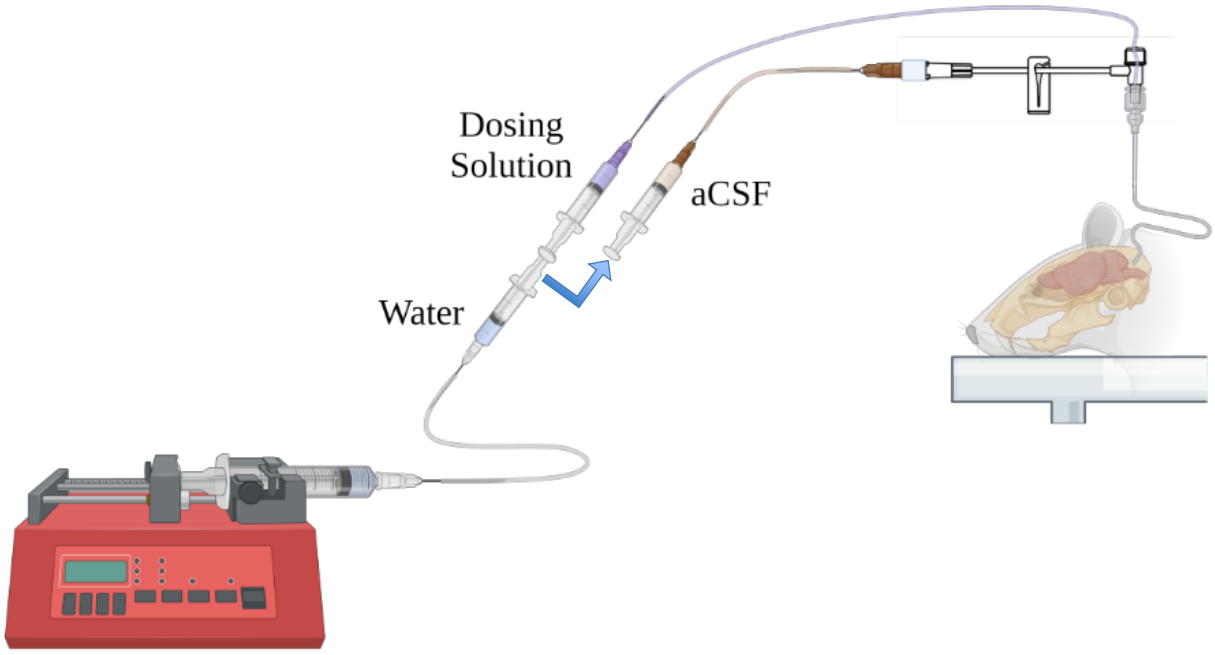

Figure 10: Schematic of catheters for ICM IT instillation. A schematic showing how catheters were constructed for the instillation of dosing solution followed by aCSF into surgically implanted ICM cannulas using a syringe pump and extender for MRI compatability.

For intrathecal administration for animals equipped with an ICM cannula, a specialized system was created for instillation (Figure 10). Due to the 16 µL dead volume of the ICM cannula, an instillation of 16 µL of artificial CSF (aCSF) was required immediately after the instillation of the dose to ensure that the dose reached the SAS. A syringe was connected to a length of PE-10 tubing with a 30G needle and hub set bevel in into the end of the tubing. A second 30G needle was set bevel into the other end and connected to a T-port with a male-male Luer adapter. The other end of the T-port was fitted with a flexible plastic 20G catheter. To create the second channel, a length of PE-10 tubing was fed through the rubber hub of the T-port and into the 20G catheter. This apparatus was connected to a syringe pump via a closed circuit of two syringes connected with a catheter and filled with water. By butting the ends of the dosing syringe and the water syringe together, the depression of the water syringe in the pump caused the water syringe adjacent to the dosing syringe to expand by the same amount, which then depressed the dosing syringe. This allowed the syringe pump itself to be placed a safe distance from the MRI.

Animals were anesthetized with isoflurane. The animal's eyes were lubricated, and each animal was brought to a baseline level of hydration with an IP injection of 2 mL of sterile saline. Animals were subsequently placed in a prone position on a HT bed. Scans were executed with continuous monitoring of the animals' physiological parameters.

Once in the scanner, animal placement was confirmed with a localizer scan, and simultaneous PET/MR images were acquired at the desired timepoints. Reconstruction methods were maintained from the previous experiments.

3.2.7.2. IN Condition

The setup for IN dosing amd animal monitoring methods were maintained from previous experiments. Like the previous intranasal experiemnt, a sufficiently long catheter was used to allow for dynamic PET/MR scanning of dosing. In this experiment, dosing was achieved by using a syringe pump to alternate between dosing 10 µL over 30 seconds with no dosing for 30 seconds until a total of 50 µL had been administered, using the previously described syringe pump extension mechanism (Figure 11).

Once in the scanner, animal placement was confirmed with a localizer scan, and simultaneous PET/MR images were acquired at the desired timepoints. Reconstruction methods were maintained from the previous experiments.

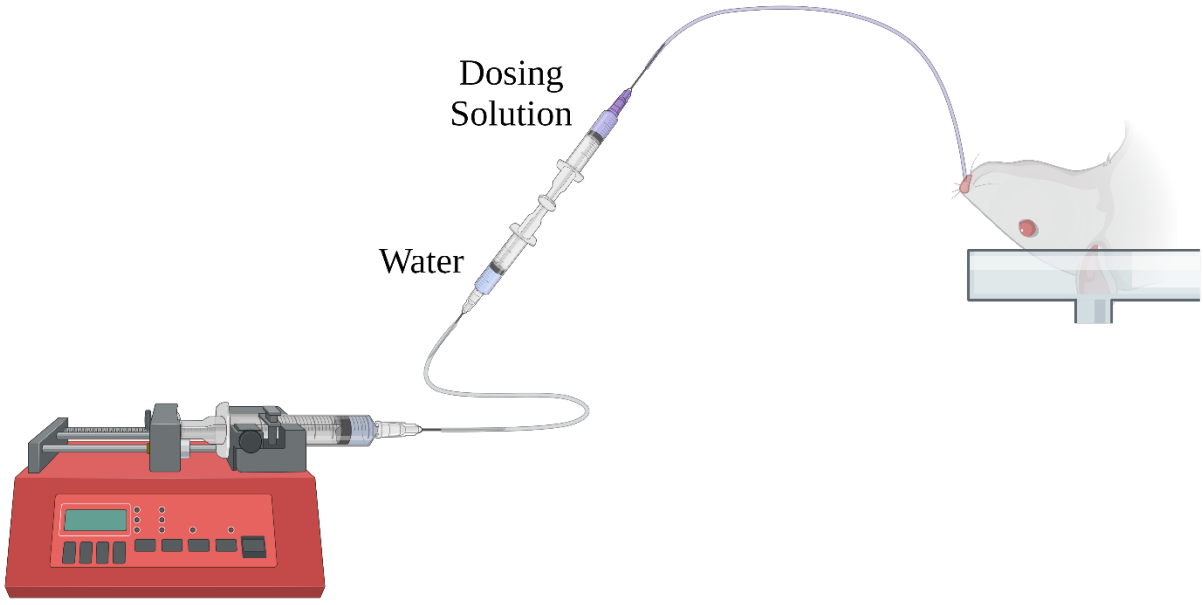

Figure 11: Schematic of catheters for IN instillation. A schematic showing how catheters were constructed for the instillation of dosing solution into the nasal cavity while maintaining a safe distance between the MRI and the syringe pump.

3.2.7.3. IV Condition

For intravenous injection of ^{18}F-FDS, animals were anesthetized with isoflurane. The animal's eyes were lubricated, and each animal was brought to a baseline level of hydration with an IP injection of 2 mL of sterile saline. The tail was cleaned with an alcohol swab to disinfect the area and improve vein visibility. The lateral tail vein, which runs along the sides of the tail, was located. A catheter filled with saline solution was inserted into the tail vein at a shallow angle (15-30 degrees) with the bevel facing up. The catheter was slowly advanced into the vein. A flash of blood in the catheter hub indicated that the vein had been successfully accessed. Once the catheter was securely in place, the syringe containing the ^{18}F-FDS solution was attached to the catheter for dosing.

The syringe plunger was gently depressed to inject the ^{18}F-FDS solution, injecting slowly to avoid rupturing the vein. If resistance was felt or if the area around the injection site swelled, the injection was stopped immediately, the catheter was withdrawn, and the injection was attempted at a different site. After dosing was complete, the catheter was flushed with saline to ensure that the entire dose had been administered and to maintain

catheter patency. Using a sufficiently long catheter, this procedure was completed while the animal was being scanned to obtain dynamic dosing information after a localizer scan confirmed proper placement in the scanner. Reconstruction methods were maintained from the previous experiments.

3.2.8. Lymphatic ligation surgery

Rodents were anesthetized using either inhaled isoflurane. The depth of anesthesia was assessed using the toe-pinch reflex. If there was no response to the toe-pinch reflex, ophthalmic lubricant was applied to the animal's eyes. The animal was then placed in a lateral recumbant position, and its limbs were secured with surgical tape, with the top forelimb secured along the animal's side.

Analgesia was administered subcutaneously 10-20 minutes prior to surgery, using carprofen (5 mg/kg). The neck area of the animal was shaved, and any remaining hair was removed using Nair cream. The surgical site cleaned using 70% isopropanol. Lidocaine (up to 4 mg/kg) was then infiltrated along the incision line.

The animal was transferred to a sterile field where the skin was cleaned again with alcohol, followed by a disinfectant skin preparation using alternating applications of betadine and chlorhexidine (three times each), from the center of the surgical site to the periphery.

Wearing sterile gloves, gown, and mask, the surgeon made a lateral incision in the neck, anterior to the apex of the scapula, with a sterile scalpel. The sternocleidomastoid muscles were retracted using forceps to expose the deep cervical lymph nodes. Afferent lymphatic vessels were isolated using blunt dissection and ligated with braided, non-absorbable sutures (5-0 to 10-0).

If muscle tissue was disrupted, absorbable sutures (3-0 to 5-0) were used to close the dead space. The skin at the incision site was then closed using both cuticular and cutaneous closures with absorbable sutures (3-0 to 5-0). This procedure was then repeated on the other side of the animal. Warm saline (up to 3 mL) was injected subcutaneously to replenish fluids lost during the operation.

Following the surgery, the animal was allowed to recover on a heating pad in appropriate caging and monitored every 5-10 minutes until fully alert and ambulatory. Postoperative care included daily observations for three days to ensure proper recovery,

with entries recorded in the surgical records book. Analgesia was provided over the same three-day period.

3.3. Results

3.3.1. IT administration of ^{18}F-FDS in young animals

After IT injection of ^{18}F-FDS in young animals (n=8, sex balanced) and subsequent imaging at 0.5, 1.75, and 3 hours post-injection, the location of activity during the first post-injection scan was assessed by creating separate VOIs for the visible portion of the whole animal within the FOV, the visible portion of the spinal column, and the brain. The percentage of recovered activity within each of those VOIs is compared (Figure 12). Subject with less than 2% total activity within the CNS were excluded from further analysis. PET/MR image arrays from representative included and excluded animals show visible activity within the brain VOI of the included animal and activity rostral to the brain and dorsal to the spinal cord in the excluded animal (Figure 13).

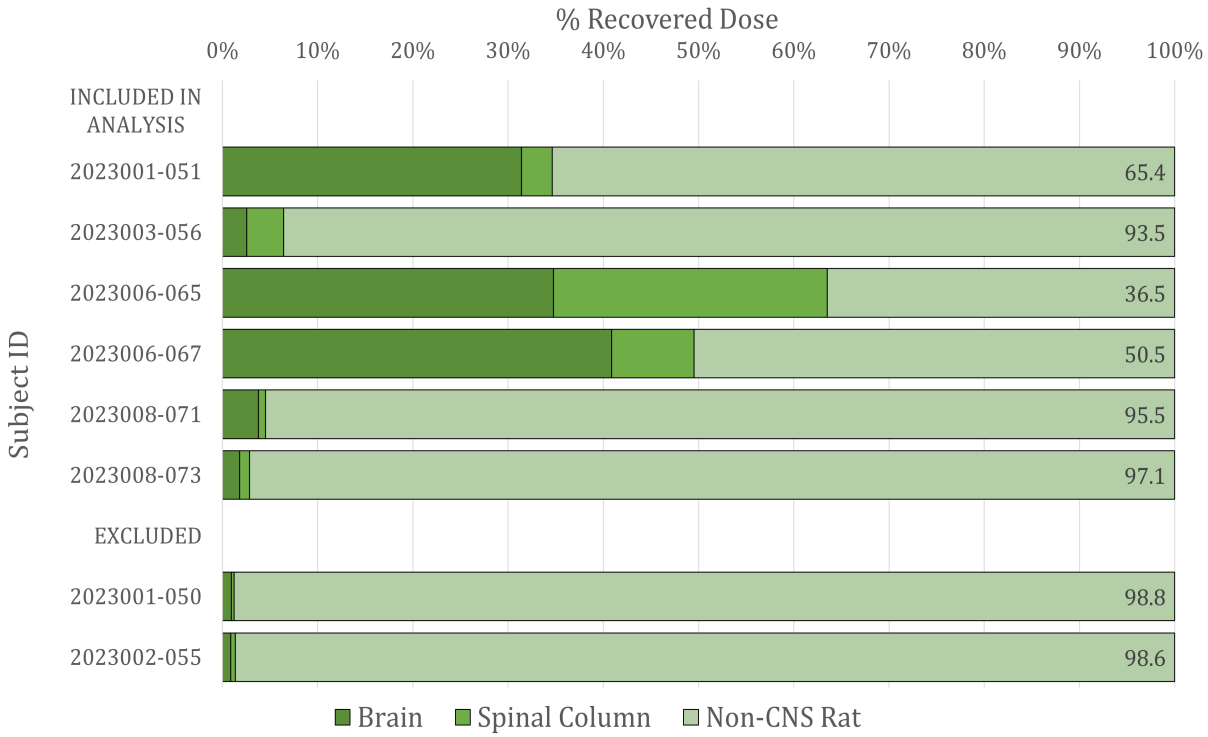

Figure 12: Assessment of activity location after IT injection in young animals. The location of activity (% recovered dose) of individual 6-month-old subjects (n=8, sex balanced) was assessed 30 minutes post-injection.

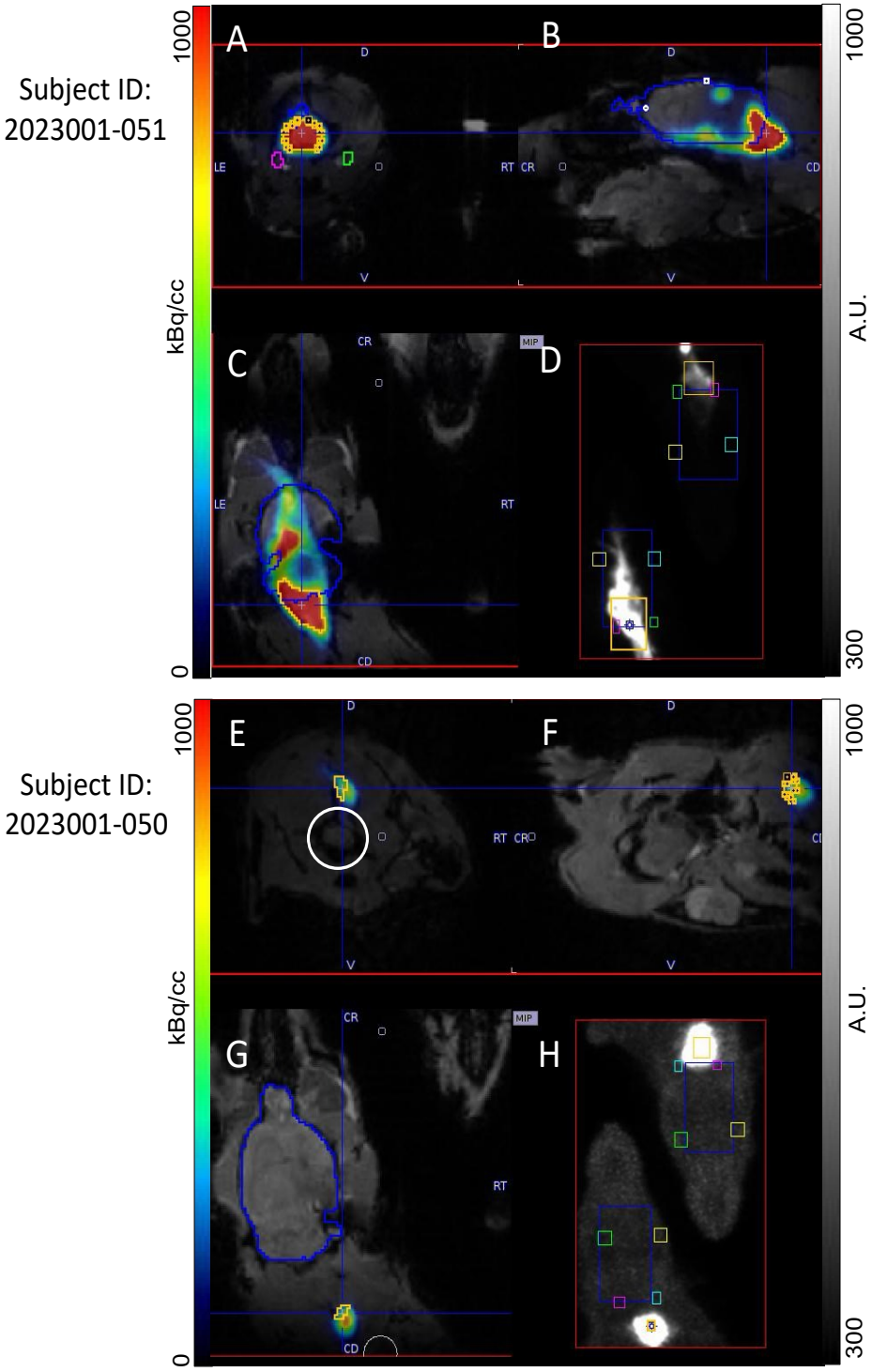

Figure 13: Representative images of varied injection quality. PET/MR images from two representative animals, one that was included in further analysis (A-D) and one that was excluded from further analysis (E-H). Each image array shows a coronal (A, E) sagittal (B, F), and transverse (C, G) view as well as a maximum intensity projection (MIP) (D, H). In the included animal, significant activity can be seen within the brain (blue VOI). In the excluded animal, activity can been seen rostral to the brain and dorsal to the spinal cord (white circle in E).

The slope between timepoints was assessed and compared between imaging groups (**Error! Reference source not found.**). The change in activity between the first and second t imepoint of the 0-4 HPI imaging session (0.5-1.75 HPI) was significantly greater than the change in activity between the first and second timepoint of the 4-8 HPI imaging session (4.25-5.5 HPI). No significant difference was observed when the slopes between later timepoints was comared.

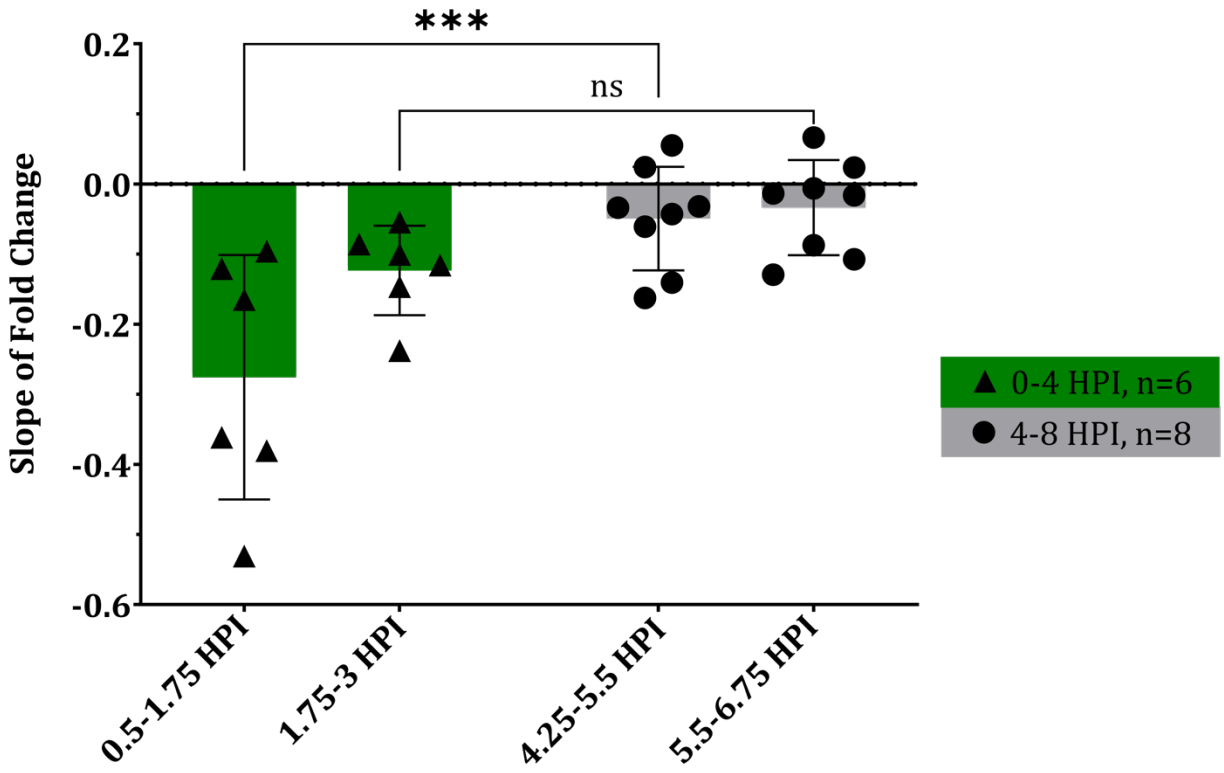

Figure 14: Tracer Clearance Dynamics Between 0–4 and 4–8 Hour Timepoints. The slope between timepoints was assessed. The change in activity between 0.5 and 1.75 hours post-injection (HPI) was significantly greater than between 4.25 and 5.5 HPI. No significant difference was observed between the 1.75–3 HPI and 5.5–6.75 HPI intervals.

Analysis of subject with greater than 2% recovered activity within the CNS (n=6, 4 female and 2 male) showed results showed a statistically significant fold decrease in all VOIs of interest across all timepoints, when compared to the first measured activity (Figure 15). When visualized with PET, using MR for anatomical reference (Figure 16), a localization of activity can be seen within the CNS at the injection site, the cisterna magna. Subsequent timepoints depict clearance of activity away from this area.

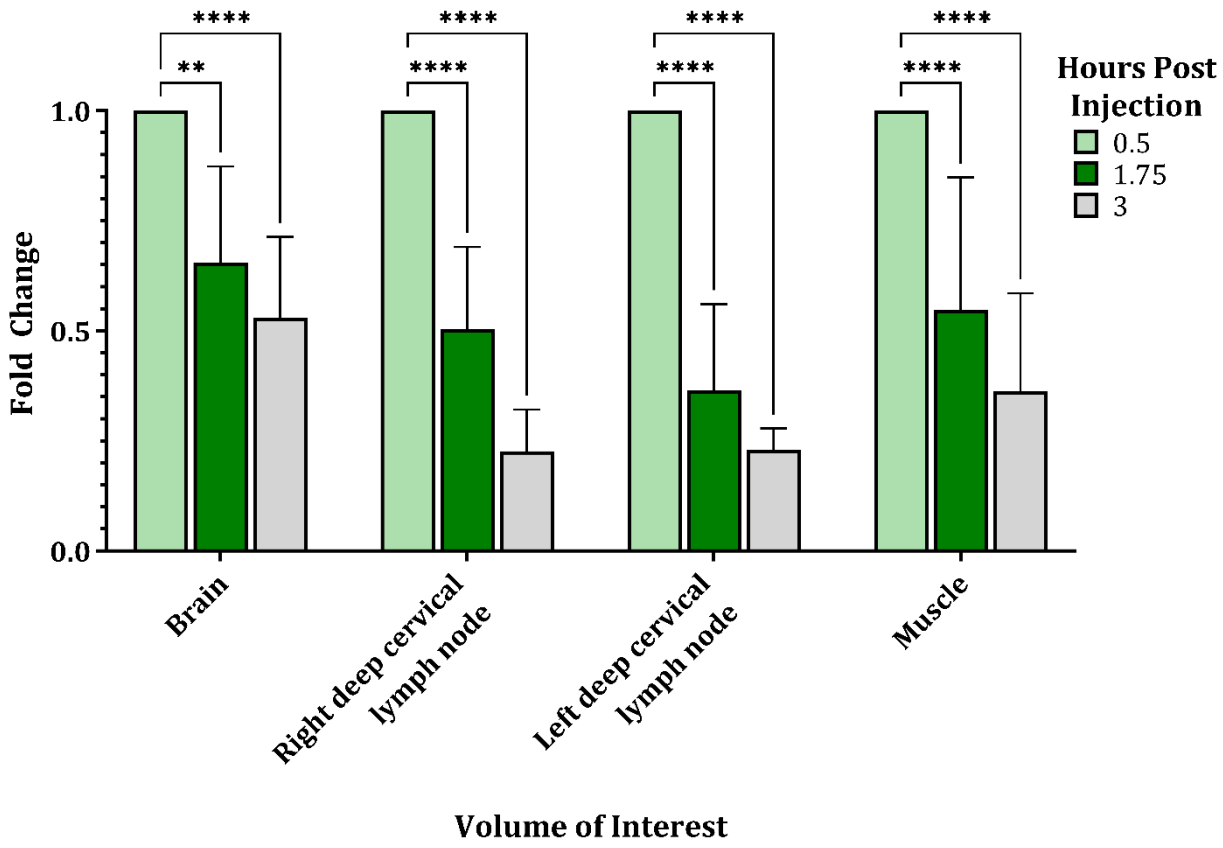

Figure 15: Graph of ^{18}F-FDS clearance after IT injection in young rats. The averaged fold change was calculated from initial activity (kBq) per volume of interest for 6-month-old animals (n=6, 2 male and 4 female) across all timepoints. Averaged ^{18}F-FDS activity decreased significantly when compared to the respective initial scan average in all VOIs.

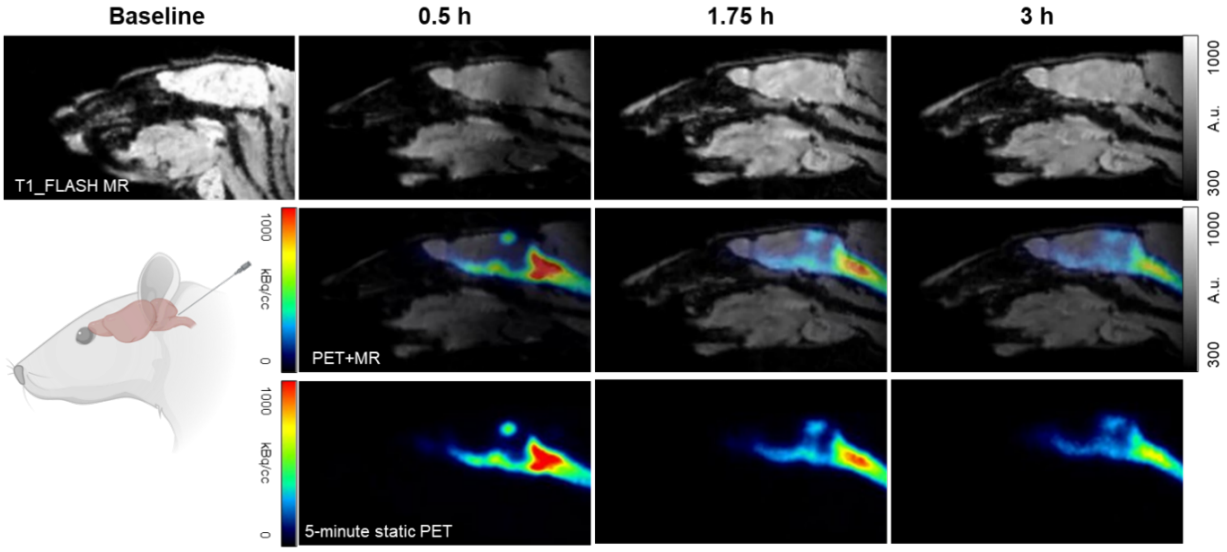

Figure 16: Images of ^{18}F-FDS clearance after IT injection in a young rat. An image series is shown for a representative animal (6-month-old female): MR T1_FLASH images are shown in the top row, combined PET+MR images are shown in the middle row, and 5-minute static PET scans are shown in the bottom row. ^{18}F-FDS activity was initially localized at the injection site and showed clearance over time.

3.3.2. IT administration of ^{18}F-FDS in aged animals

Aged animals (n=2, male) were injected with ^{18}F-FDS IT and subsequently imaged at 0.5, 1.75, and 3 hours post-injection. Fold change from initial activity (kBq) was calculated. Due to the sample size, statistical significance could not be assessed (Figure 17). When PET/MR images of a representative animal are shown, minimal clearance away from the injection site is seen over time (Figure 18).

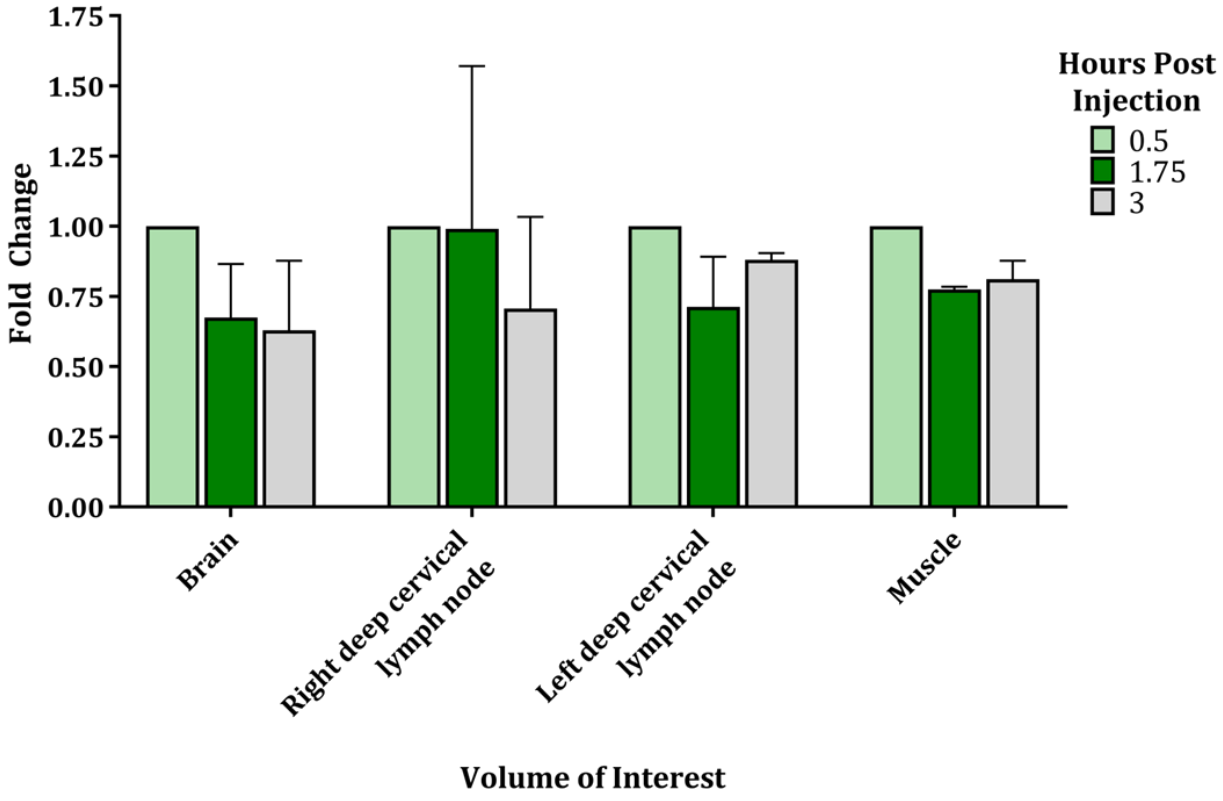

Figure 17: Graph of ^{18}F-FDS clearance after IT injection in aged animals. The averaged fold change was calculated from initial activity (kBq) per volume of interest for 27-month-old animals (n=2, male) across all timepoints.

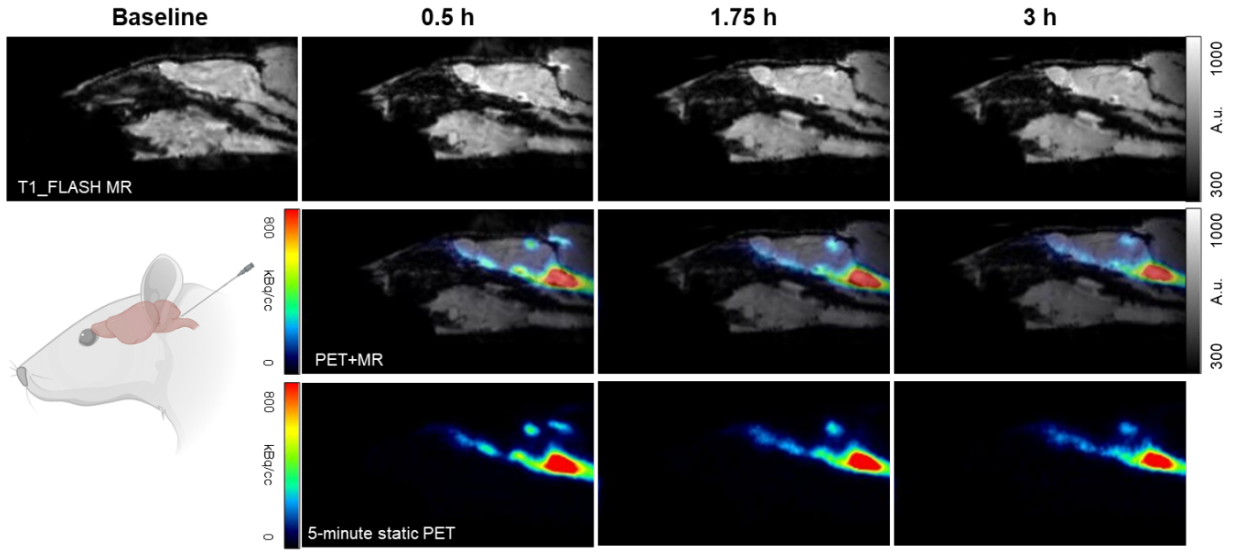

Figure 18: Images of ^{18}F-FDS clearance after IT injection in aged animals. An image series is shown for a representative animal: MR T1_FLASH images are shown in the top row, combined PET+MR images are shown in the middle row, and 5-minute static PET scans are shown in the bottom row. ^{18}F-FDS activity was initially localized at the injection site and showed very little change time.

3.3.3. Biodistribution of ^{18}F-FDS activity after IT injection

The biodistribution of ^{18}F-FDS after IT injection was assessed by sacrificing middle-aged animals (n=3, 17-month-old males) one hour after IT injection of ^{18}F-FDS. All relavant tissues were immediately removed and placed into pre-weighed vials. The activity (CPM) of each excised tissue was assessed with a gamma counter calibrated for ^{18}F (Figure 19). Increased activity per gram of tissue was seen in the kidneys and brain.

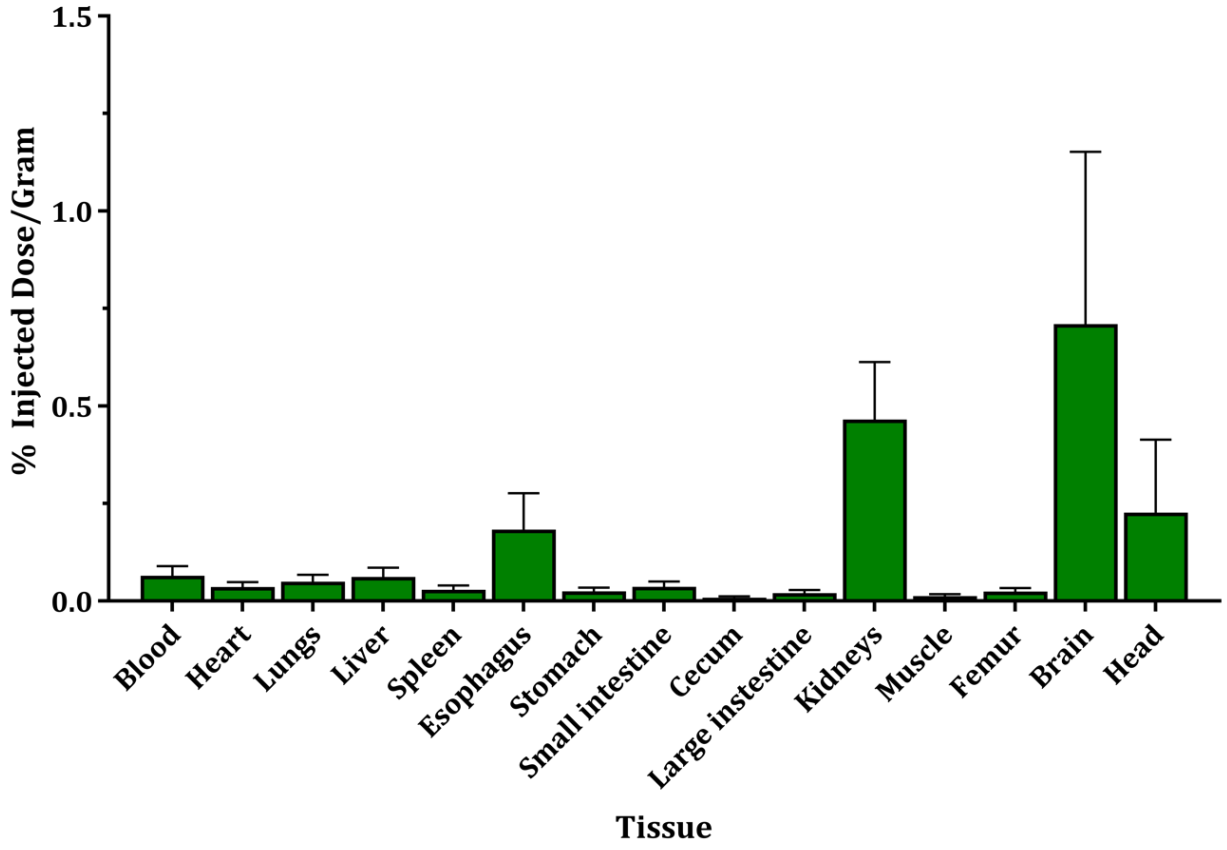

Figure 19: Assessment of ^{18}F-FDS biodistribution after IT injection. Middle aged (17-month-old) animals (n=3, male) were injected with ^{18}F-FDS IT and sacrificied 1 hour post-injection. Tissues were immdiately excised and activity (CPM) was measured in a gamma counter.

3.3.4. IN instillation of ^{18}F-FDS with versus without absorption enhancers

The time activity curves (TAC) of ^{18}F-FDS brain activity (SUV) (n=2, sex balanced) were compared the TAC of ^{18}F-FDS with 0.25% w/v DDM (n=2, sex balanced) and ^{18}F-FDS with 0.25% w/v TDM (n=2, sex balanced). The activity of ^{18}F-FDS in the brain was measured every 30 seconds for 10 minutes three times, at approxiamtely 0 minutes, 60 minutes, and 100 minutes after injection. Exact timing of imaging is reflected in the graph (Figure 20). When PET/MR images of the study are viewed orthogonally (note the supine position of the subject), large amounts of activity can still be seen in the nasal cavity more than an hour after IN instillation (Figure 21). When only the activity within the brain VOI is viewed, activity can be visualized at the olfactory bulb and at the basal aspect of the brain (Figure 22).

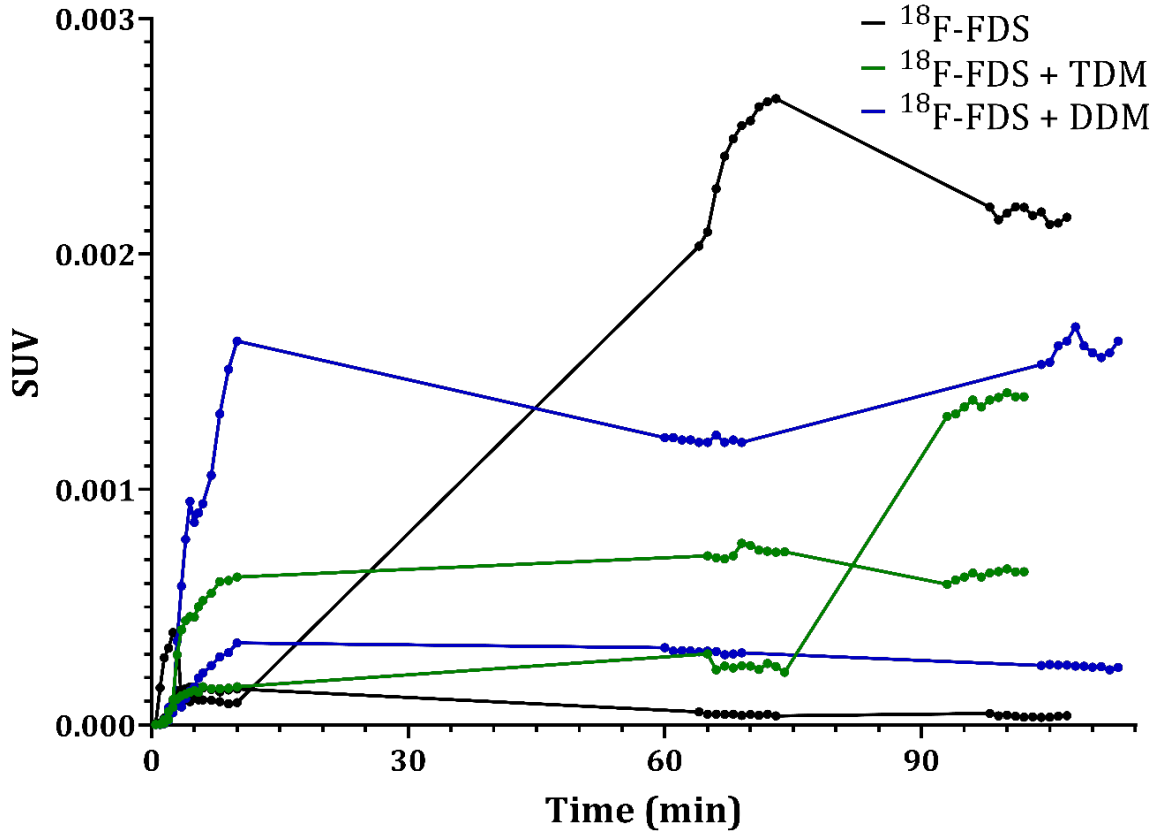

Figure 20: Brain actvity (SUV) following IN instillation of ^{18}F-FDS in control versus TDM and DDM conditions. Time activity curves of ^{18}F-FDS brain activity (SUV) were compared between ^{18}F-FDS alone, ^{18}F-FDS with 0.25% w/v DDM, and ^{18}F-FDS with 0.25% w/v TDM (n=6, 2 per group, sex-balanced). Brain activity was measured every 30 seconds for 10 minutes at approximately 0, 60, and 100 minutes post-injection.

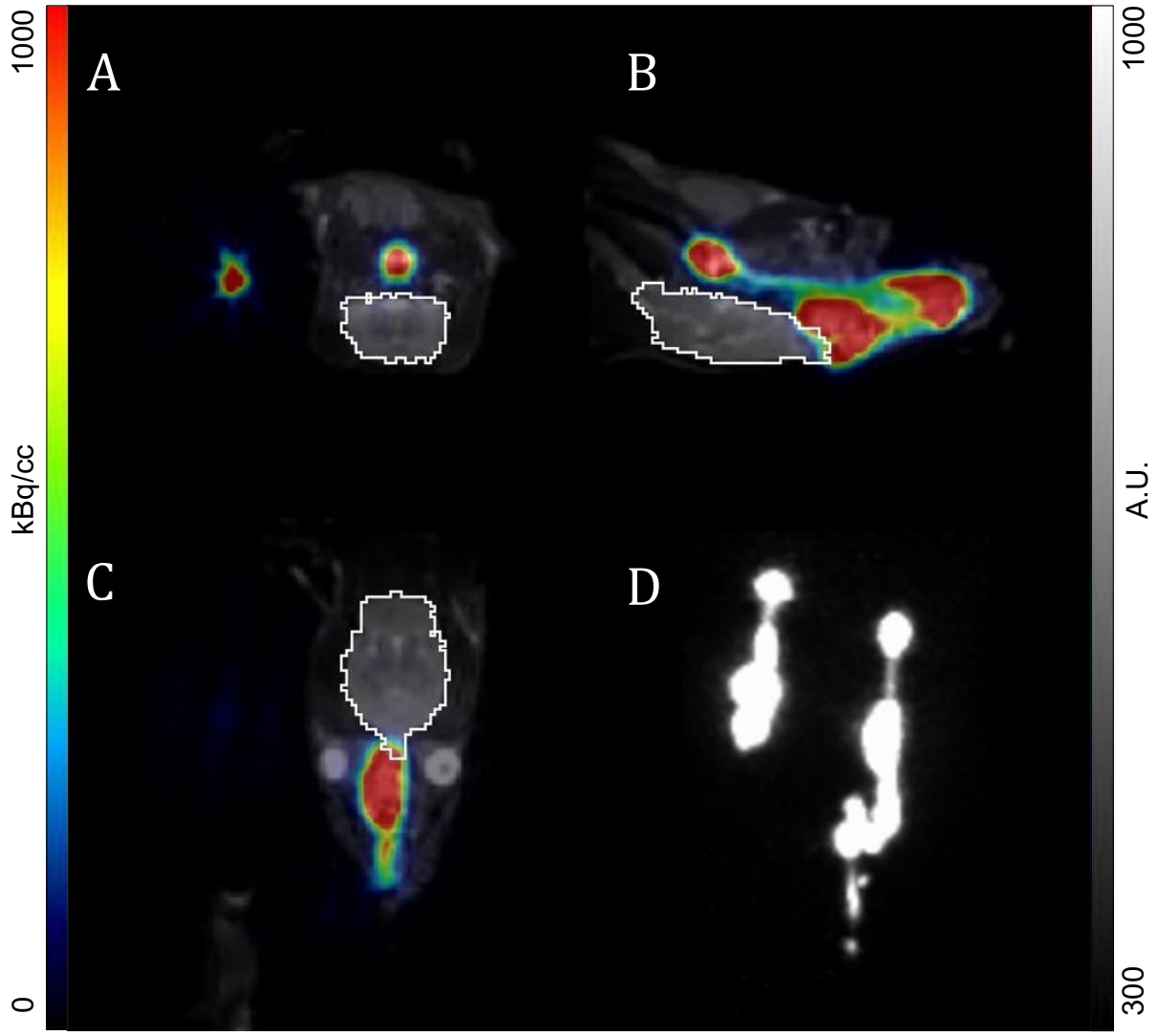

Figure 21: Orthogonal view of 65-minute post IN instillation of ^{18}F-FDS. Panels A-C show PET activity (color scale) with MR (greyscale) for anatomical reference to illustrate the distribution of activity within the animal 65 minutes after IN instillation of ^{18}F-FDS. Panel D shows the MIP for the activity within the FOV with the subject of interest on the right.

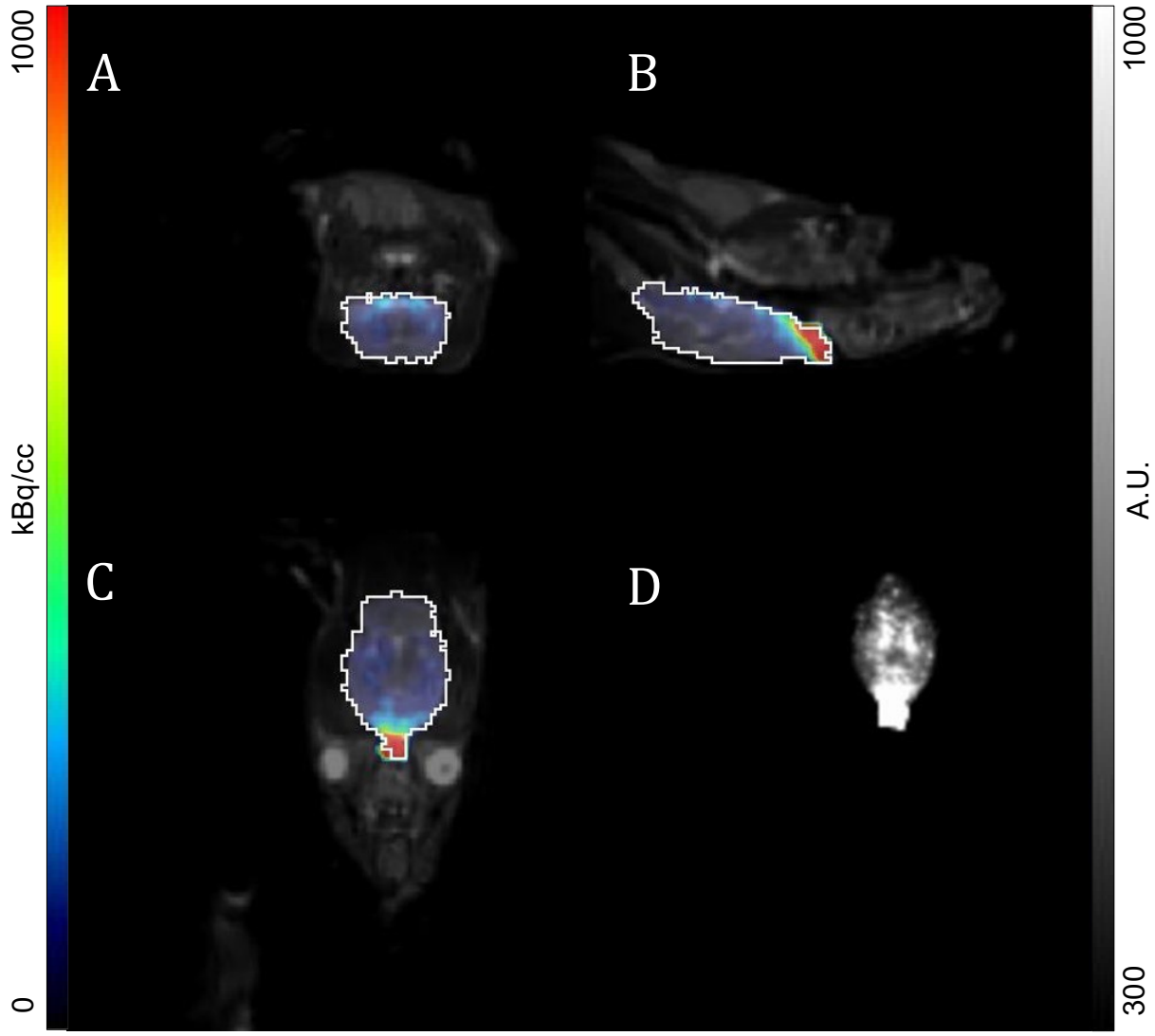

Figure 22: Orthogonal view of 65-minute post IN instillation of ^{18}F-FDS. Panels A-C show PET activity (color scale) restricted to the Brain VOI (white) with MR (greyscale) for anatomical reference to illustrate the distribution of activity within the brain 65 minutes after IN instillation of ^{18}F-FDS. Panel D shows the MIP for the brain VOI.

3.3.5. Comparison of routes of ^{18}F-FDS administration

Averaged TAC of the brain following ^{18}F-FDS administration are used to compare IT (n=2), IN (n=2), and IV (n=3) administration in 4-month-old female Sprague-Dawley rats. All groups were imaged dynamically from 0 to 45 minutes post-administration, followed by at least two additional imaging sessions extending to at least 200 minutes post-administration (Figure 23). Brain activity was about 100 times higher in IN subjects as compared to IT subjects. IV brain activity was approximately half that of IN activity. Time to peak activity (TTP) (min) in the brain of each subject was calculated and routes of administration were compared (Table 4). The averaged TTP for IV subjects was the shortest at only 4.5 ± 1.0 min (n=3), followed by IT at 18.5 ± 0.0 min (n=2). IN subjects did not peak on average until 27.5 ± 5.00 min (n=2). PET signal in the brain was normalized as the percentage of the maximum total PET signal at time t relative to the total PET signal at an initial reference time t_1 after IT (n=2), IN (n=2) and IV (n=3) (Figure 24).

Orthogonal PET/MR images of a representative animal are shown for each route of administration (Figure 28, Figure 30, Figure 32). Signal only within the brain VOI was visualized to allow for a better understanding of activity distribution in that location, especially for those conditions with lower activity (Figure 29, Figure 31, Figure 33).

Route of Administration	N	Time to Peak (min ± SE)
Intranasal	2	27.5 ± 5.00
Intrathecal	2	27.5 ± 0.00
Intravenous	3	4.5 ± 1.00

Table 4: Comparison of routes of administration using time to peak. Time to peak (TTP) for individual TAC (kBq/cc) was calculated and averaged for each dosing condition (min ± SE).

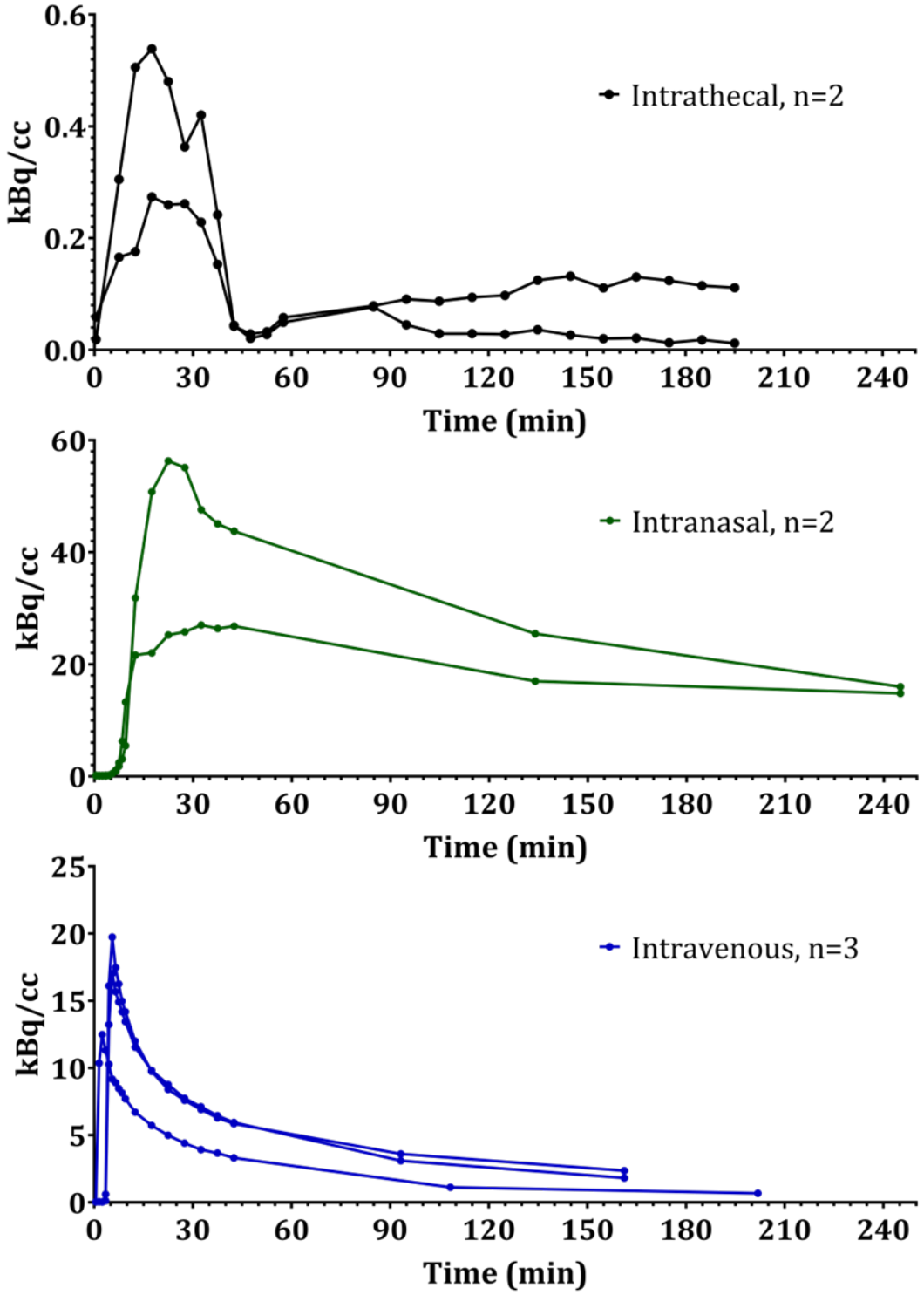

Figure 23: Comparison of brain TAC for IT, IV, and IN administration. TAC for the brain after IT (n=2), IN (n=2), or IV (n=3) administration of ^{18}F-FDS in female Sprague-Dawley rats are shown. Imaging was continous for 0-45 minutes post-dose for all groups, in addition to varied timepoints until approximately 200 minutes.

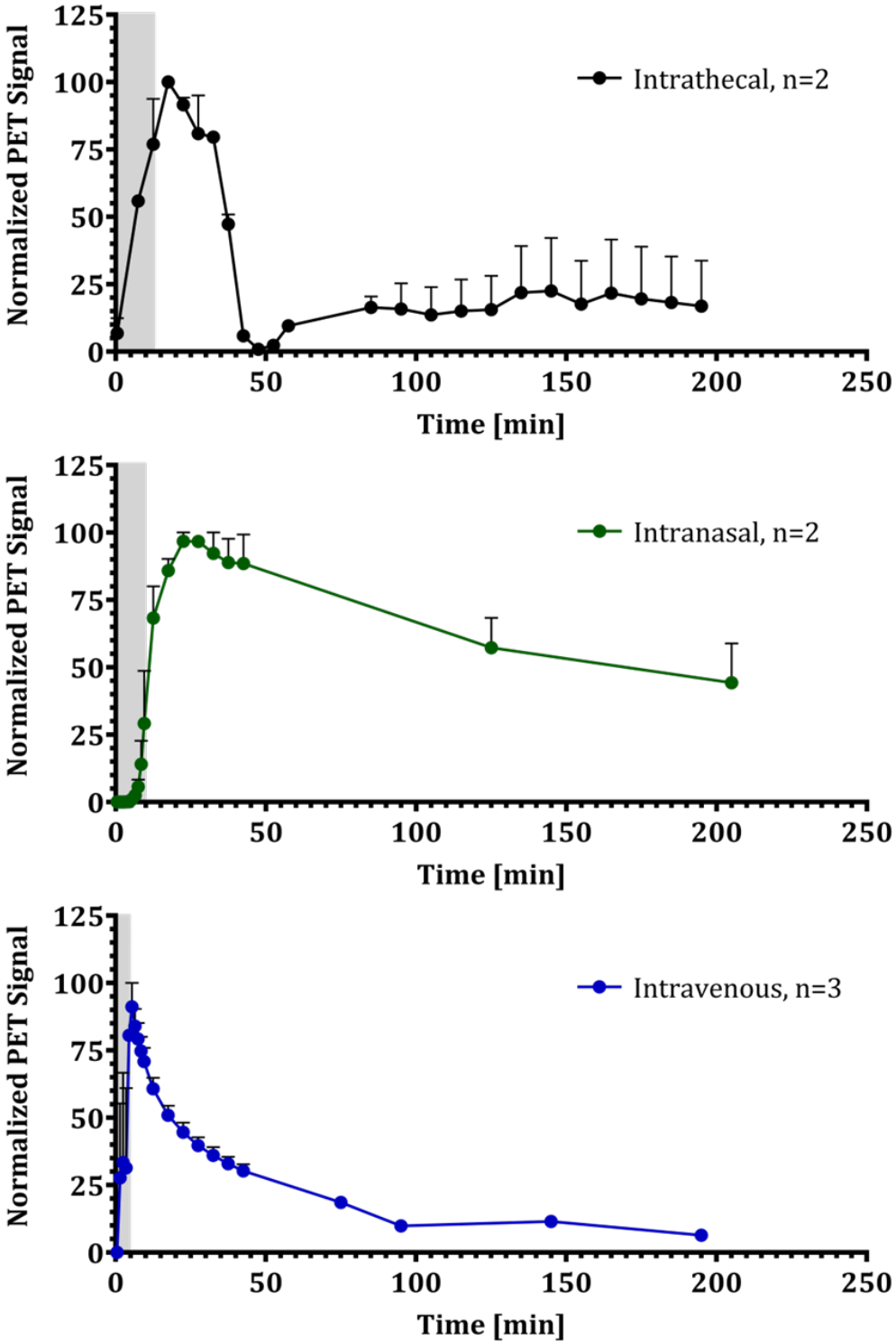

Figure 24: Normalized PET brain signal after ^{18}F-FDS administration. Averaged TAC (normalized PET signal) for the brain VOI after IT (n=2), IN (n=2) and IV (n=3) administration are shown for each young female Sprague-Dawley rat. Duration of dosing is indicated by the width of the grey box.

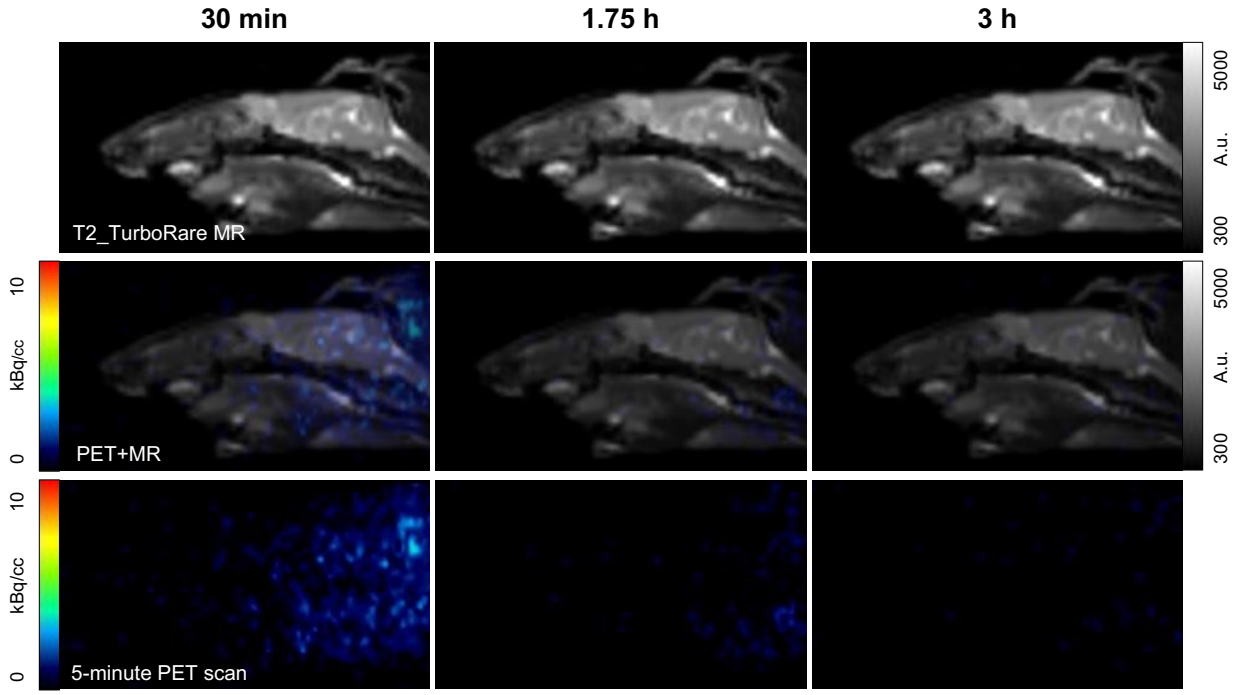

Figure 25: Images of ^{18}F-FDS clearance after IT instillation through ICM cannula in a young rat. An image series is shown for a representative animal (4-month-old female) depicting change in activity over time: MR T2_TurboRARE images are shown in the top row, combined PET+MR images are shown in the middle row, and 5-minute PET scans are

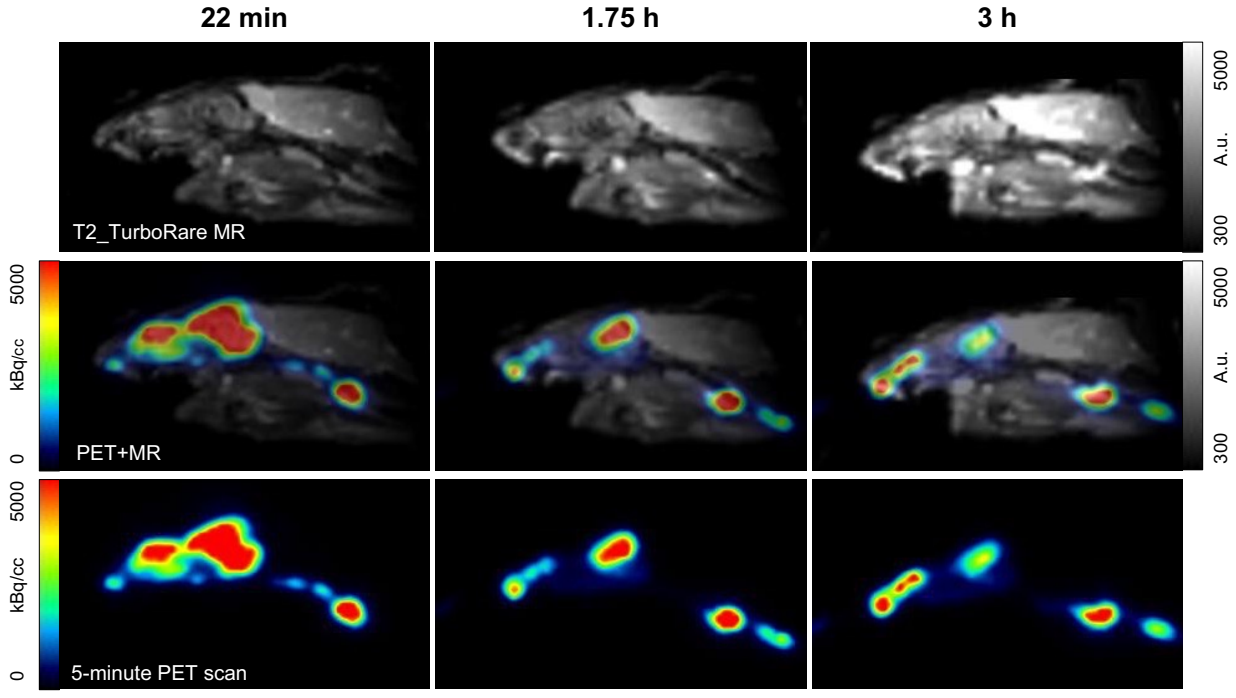

Figure 26: *Images of ^{18}F-FDS clearance after IN instillation in a young rat.* An image series is shown for a representative animal (4-month-old female) depicting change in activity over time: MR T2_TurboRARE images are shown in the top row, combined PET+MR images are

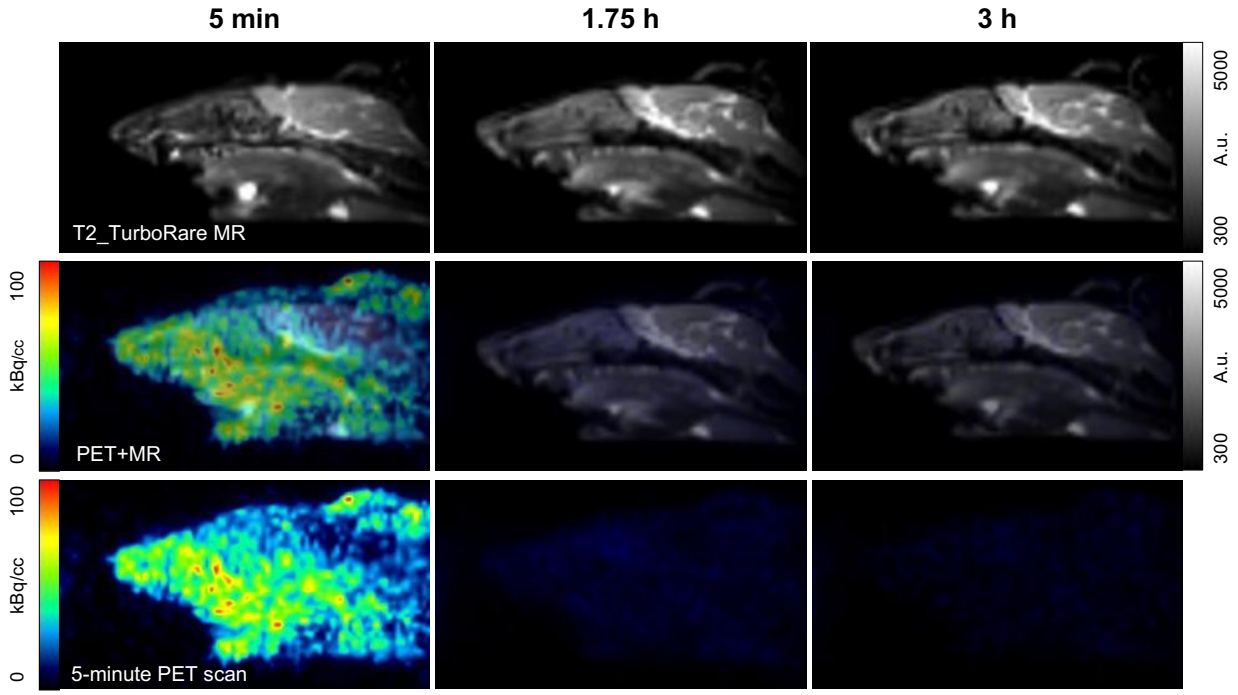

Figure 27: *Images of ^{18}F-FDS clearance after IV administration in a young rat.* An image series is shown for a representative animal (4-month-old female) depicting change in activity over time: MR T2_TurboRARE images are shown in the top row, combined PET+MR images are shown in the middle row, and 5-minute PET scans are shown in the bottom row.

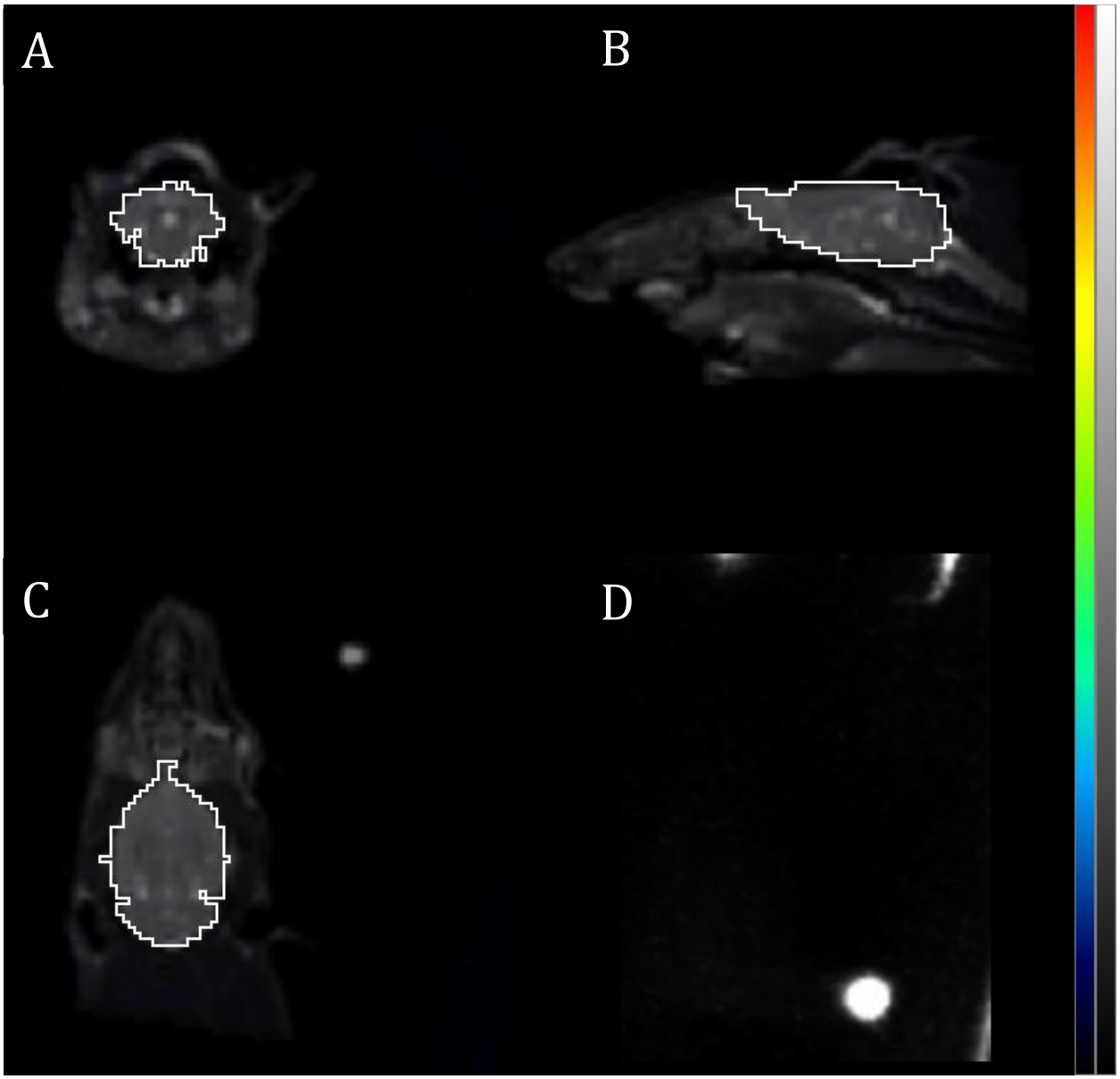

Figure 28: Orthogonal view of 20-minute post IT instillation of ^{18}F-FDS via cannula. Panels A-C show PET activity (color scale) with MR (greyscale) for anatomical reference to illustrate the distribution of activity within the animal 20 minutes after IT instillation of ^{18}F-FDS. Panel D shows the MIP for the activity within the FOV.

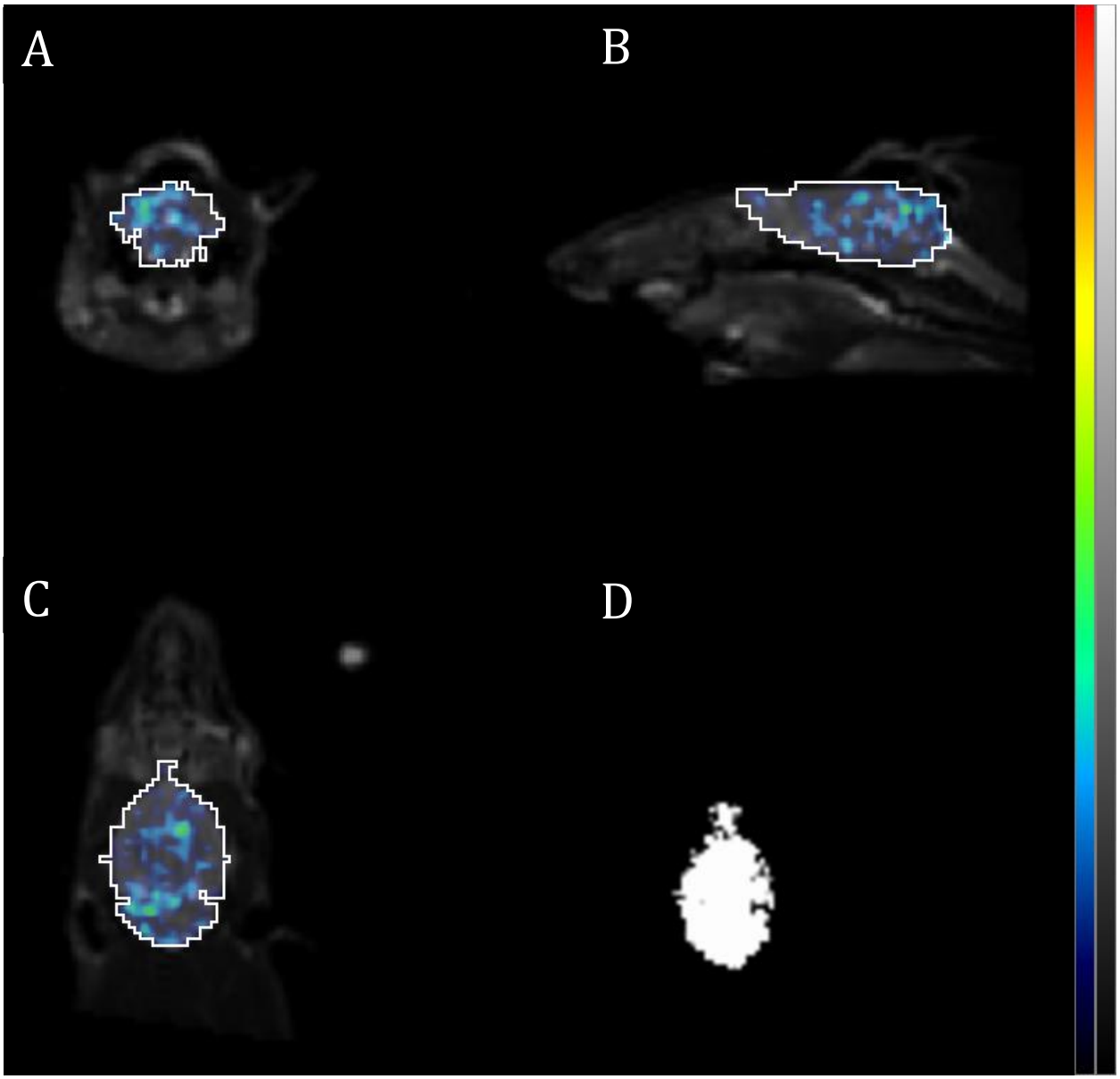

Figure 29: Orthogonal view of 20-minute post IT instillation of ^{18}F-FDS via cannula. Panels A-C show PET activity (color scale) restricted to brain VOI (white) with MR (greyscale) for anatomical reference to illustrate the distribution of activity within the brain 20 minutes after IT instillation of ^{18}F-FDS. Panel D shows the MIP for the activity within the brain.

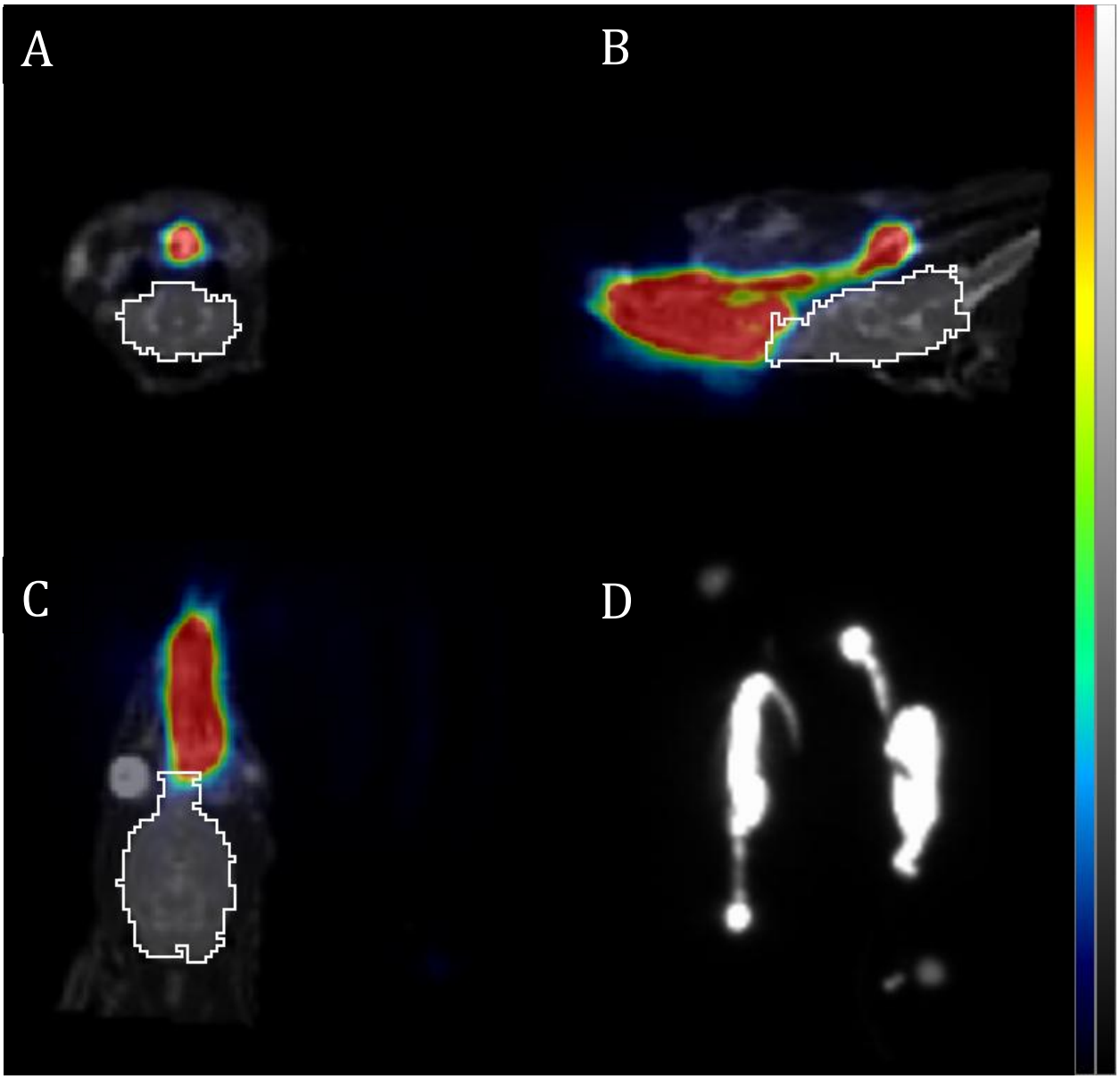

Figure 30: Orthogonal view of 20-minute post IN instillation of ^{18}F-FDS. Panels A-C show PET activity (color scale) with MR (greyscale) for anatomical reference to illustrate the distribution of activity within the animal 20 minutes after IN instillation of ^{18}F-FDS. Panel D shows the MIP for the activity within the FOV with the subject of interest on the left.

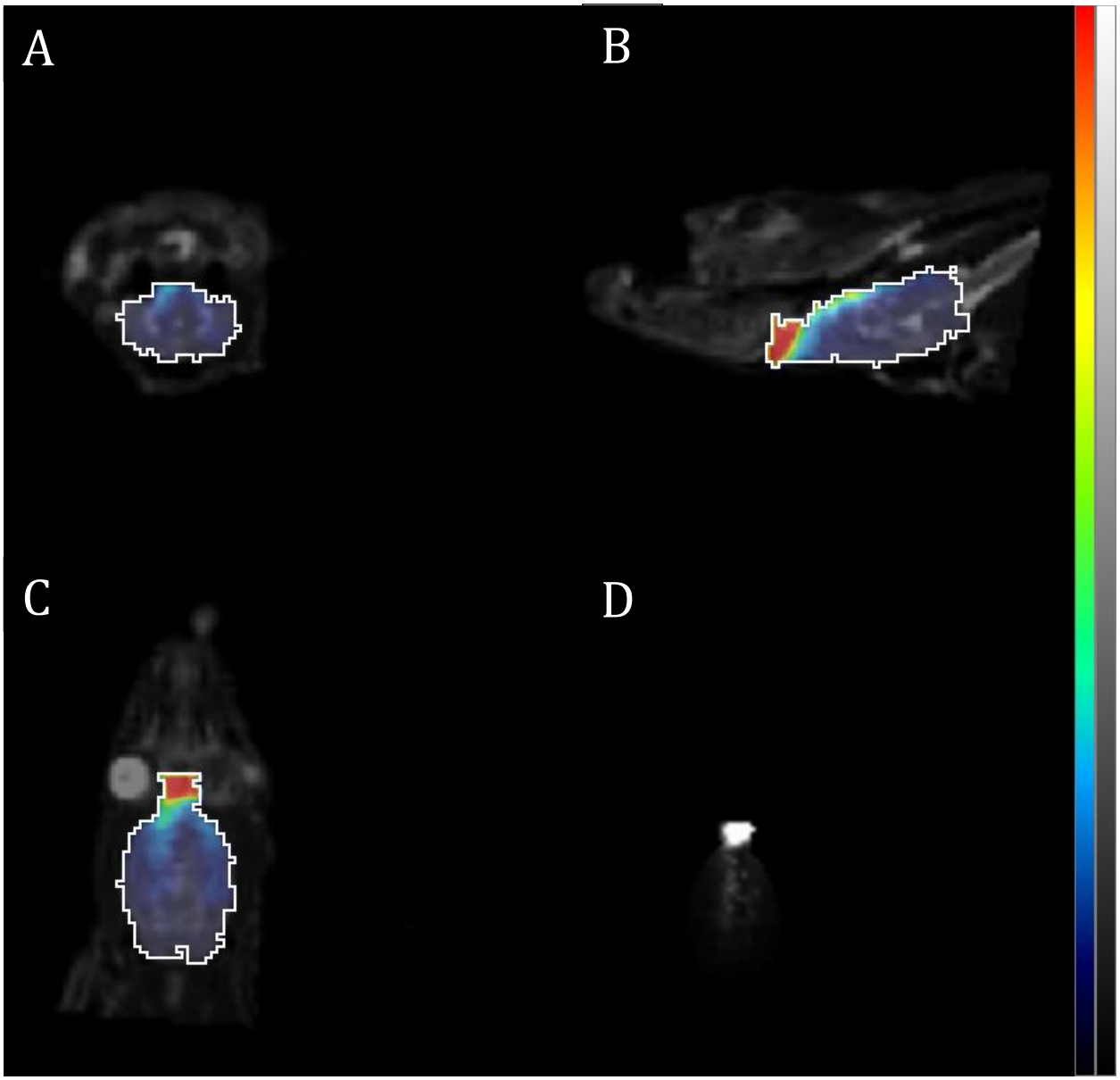

Figure 31: Orthogonal view of 20-minute post IN instillation of ^{18}F-FDS. Panels A-C show PET activity (color scale) restricted to brain VOI (white) with MR (greyscale) for anatomical reference to illustrate the distribution of activity within the brain 20 minutes after IN instillation of ^{18}F-FDS. Panel D shows the MIP for the activity within the brain.

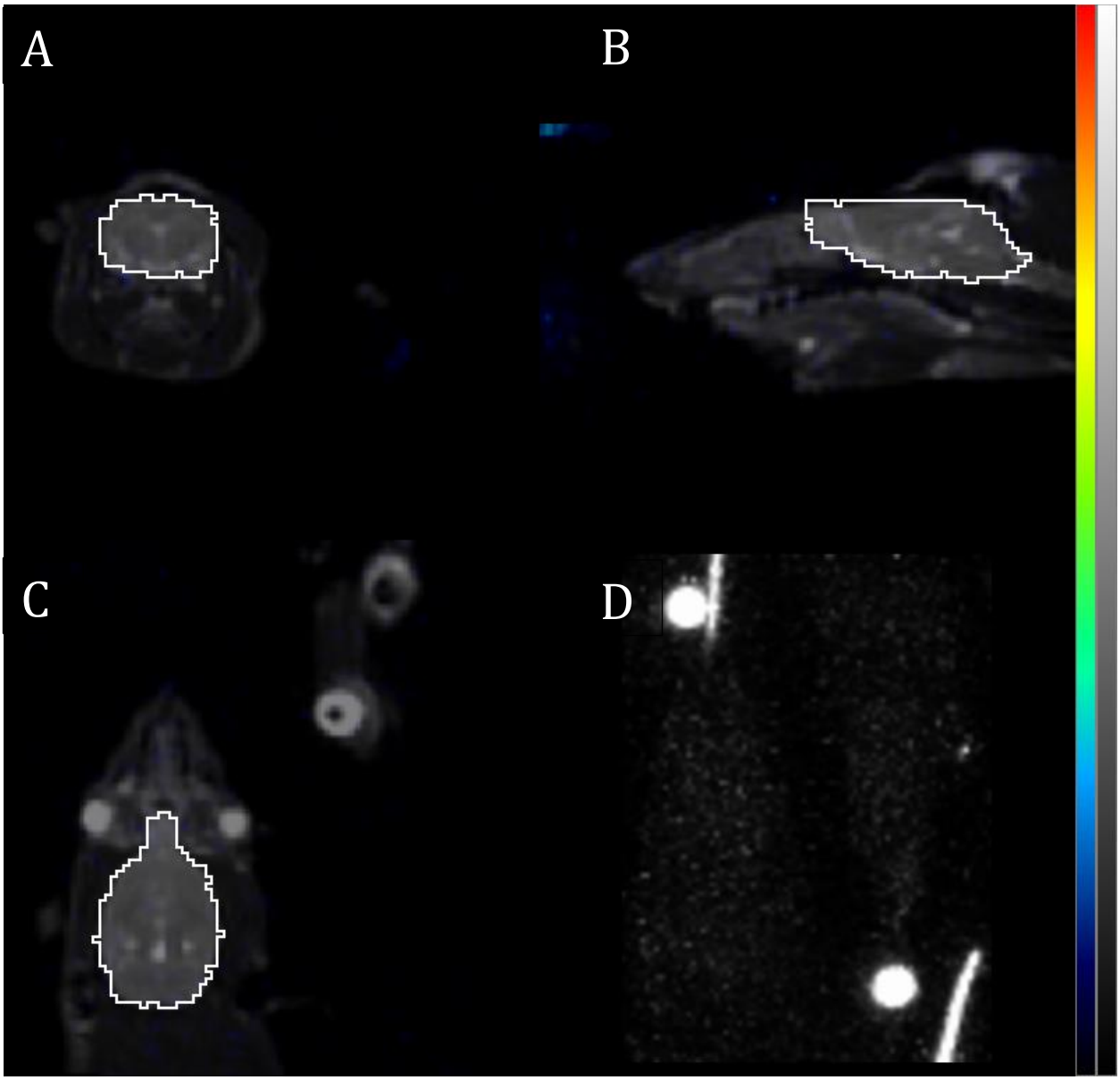

Figure 32: Orthogonal view of 20-minute post IV administration of ^{18}F-FDS. Panels A-C show PET activity (color scale) with MR (greyscale) for anatomical reference to illustrate the distribution of activity within the animal 20 minutes after IV administration of ^{18}F-FDS. Panel D shows the MIP for the activity within the FOV with the subject of interest faintly visible on the left, below the fiducial and tail of the other subject.

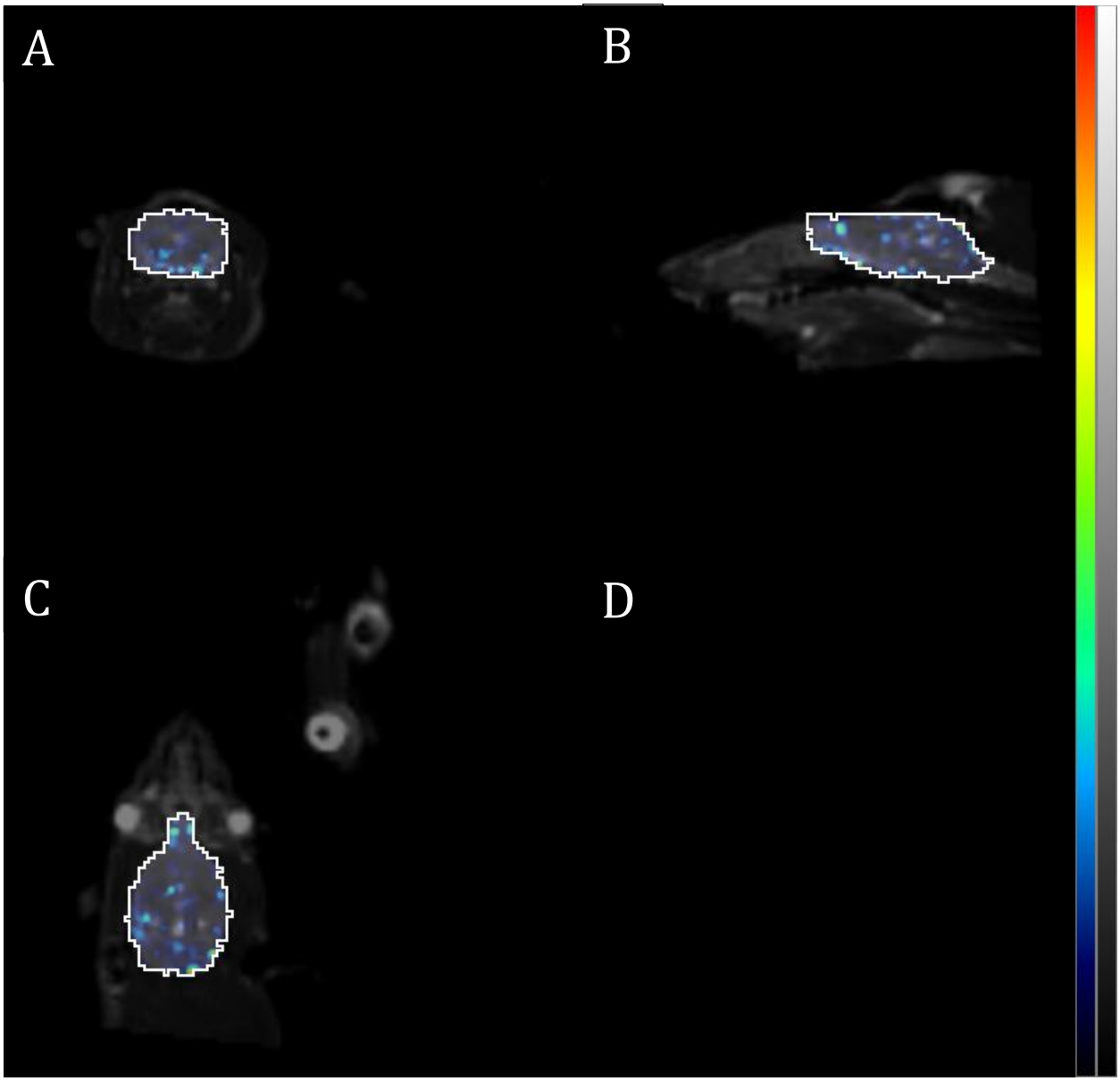

Figure 33: Orthogonal view of 20-minute post IV administration of ^{18}F-FDS. Panels A-C show PET activity (color scale) restricted to within the brain VOI (white) with MR (greyscale) for anatomical reference to illustrate the distribution of activity within the brain 20 minutes after IV administration of ^{18}F-FDS. Panel D shows the MIP for the activity within the VOI.

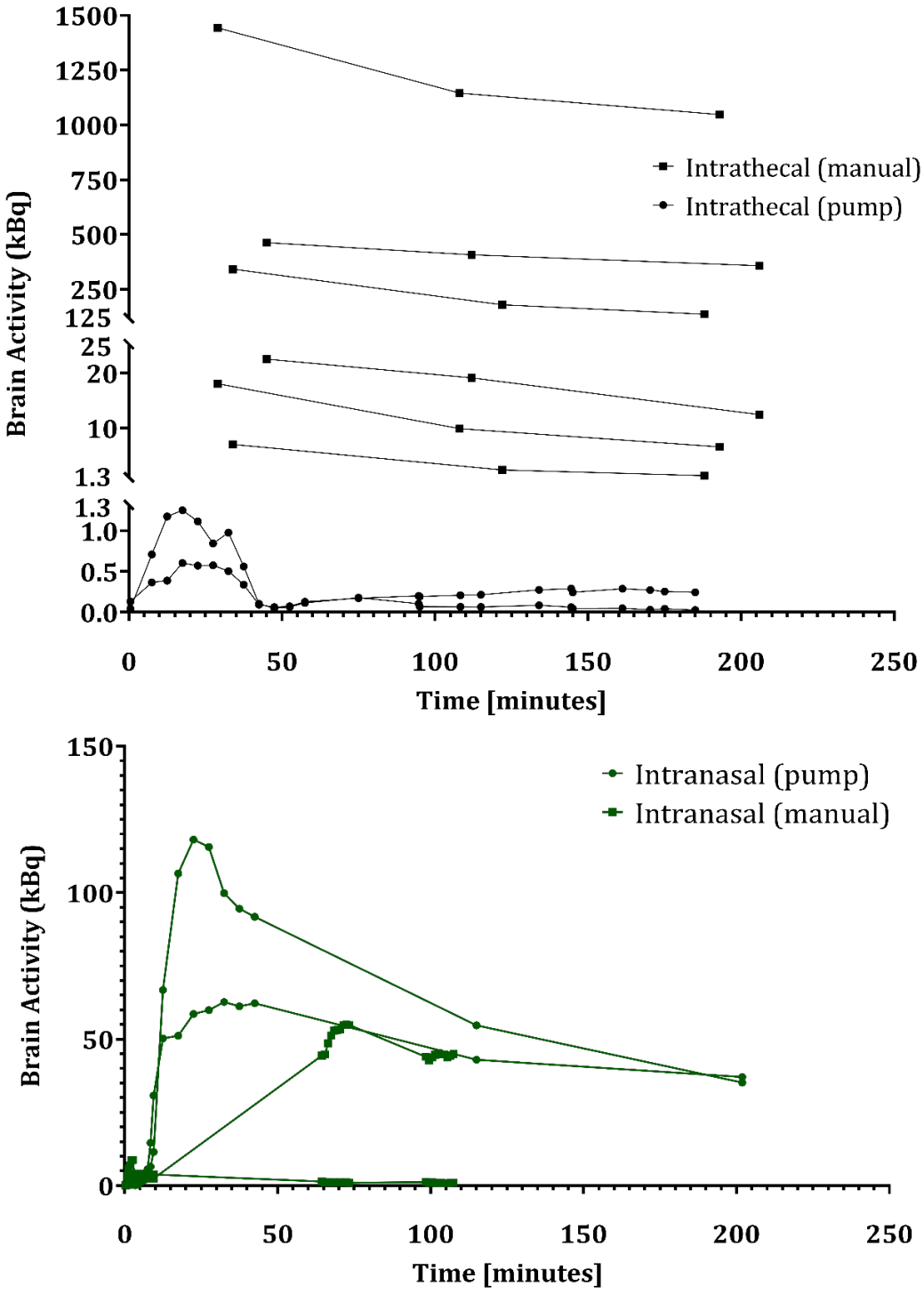

Figure 34: Aggregated TAC for IT and IN conditions. TAC of brain activity for young animal IT (n=6) and route of administration IT (n=2) data are plotted together. TAC of brain activity for IN data from absorption enhancer experiment (n=2) and route of administration comparison (n=2) are plotted together. In both graphs, square plot points indicate the use of manual needle placement (IT) or administration (IN) of tracer.

3.4. Discussion

The goal of these experiments was to assess the viability of ^{18}F-FDS as a PET tracer for the assessment of glymphatic clearance, and to identify the most desirable route of administration for translation to a clinical setting.

The quality of IT injection of ^{18}F-FDS in young animals was variable. Of the 8 animals injected for the 0-4 HPI imaging, 2 animals had less than 2% of recovered activity in the CNS. These animals were excluded from further analysis. The statistically significant difference in slope between the first 0-4 HPI timepoint and the first 4-8 HPI indicated that activity was clearing significantly faster during the 0-4 HPI imaging session than the 4-8 HPI imaging session. The slope of the change in activity between 4-8 HPI timepoints averaged to be less than -0.1, indicating that by 4 HPI, the majority of the clearance had already occurred. Because of this, data analysis was focused on the 0-4 HPI data.

Those animals who had greater than 2% of recovered activity within the CNS showed significant statistically significant clearance of the tracer at both 1.75, and 3 hours post-injection, when compared to the 0.5 hour post-injection scan. This statistically significant clearance highlights the ability of ^{18}F-FDS to act as a reliable tracer for glymphatic clearance in healthy, young animals.

However, the hand-injection method used to deliver ^{18}F-FDS to the CNS yielded variable success, limiting the sample size for analysis. Excluding animals with minimal CNS infiltration allowed for a more accurate depiction of the tracer's clearance, with results suggesting that in young animals, glymphatic clearance is both rapid and detectable using PET imaging.

No quantitiative method currently exists for assessing glymphatic clearance in a clinical setting. In this study, PET quantification was achieved through multiple metrics, including fold change in tracer concentration, activity per voxel (kBq/cc), and total activity within the volume of interest (VOI). These quantitative metrics are crucial as they provide a standardized and reproducible approach to measure glymphatic clearance, enabling objective comparisons across studies and facilitating future clinical applications. Such data-driven methods lay the foundation for developing diagnostic tools and therapeutic interventions for disorders associated with impaired glymphatic function.

The same method was repeated in aged animals. Due to a small sample size, statistical

significance could not be assessed, but a difference in trends of fold change across timepoints can be visualized on the graph (Figure 17) when compared to the same experiment performed with young animals (Figure 15). Additionally, differences in clearance can be visualized when PET/MR image arrays of representative animals are compared (Figures 16 and 18). This suggests decreased clearance and impaired glymphatic function in aged animals, supporting the hypothesis that aging is associated with a decline in glymphatic activity[4]. These results suggest that ^{18}F-FDS PET imaging may be sensitive enough to detect age-related changes in glymphatic clearance, which may have implications for the early detection of neurodegenerative diseases that are often linked to glymphatic dysfunction. The difference between young and aged animals demonstrates the potential of PET imaging as a diagnostic tool for assessing glymphatic health.

The invasive nature and variable execution of the IT injections encourged exploration of a less invasive and more consistent dosing method. IN adminitration, with brain uptake through the N2B pathway, was examined. This method was advantageous due to its non-invasive nature, which makes it more suitable for clinical translation. Delivery to the brain was tested using three formulations: ^{18}F-FDS, ^{18}F-FDS with 0.25% w/v DDM, and ^{18}F-FDS with 0.25% w/v TDM. Variability between trials was high, and no obvious trends emerged due to the inconsistent runs and low sample size. Consequently, formulations including DDM and TDM were not pursued further in subsequent trials. Although the variability in uptake reduced the reliability of these early IN experiments, the potential of IN administration as a non-invasive alternative remained promising.

A direct comparison between different routes of administration was desired to determine the most effective method for delivering ^{18}F-FDS to the CNS. The IN route boasted the highest maximum percentage of the injected dose delivered to the brain, while IV administration showed the lowest uptake, as expected, given ^{18}F-FDS's inability to cross the BBB except via the N2B pathway. The significant uptake in the IN group, along with the non-invasive nature of the method, makes this route highly desirable for clinical application. This finding aligns with the literature, which suggests that the N2B pathway is a promising avenue for drug and tracer delivery to the CNS[6].

In contrast, intravenous (IV) administration was the least effective, confirming that ^{18}F-FDS is not suitable for systemic administration due to its inability to pass the BBB. These

results underscore the importance of the route of administration in the successful delivery of tracers or drugs to the CNS[7].

To address the challenges associated with variable hand injections, specialty animals with surgically implanted ICM cannulas were used. These cannulas ensured direct delivery of 18F-FDS to the CNS via the IT route, providing a more controlled and reproducible dosing environment. However, technical issues with the syringe pump extender limited the efficacy of this method. Proper alignment of the extender was critical for dose delivery, and multiple subjects failed to receive adequate doses due to alignment errors. Even in cases where doses were successfully administered, the quantity of ^{18}F-FDS delivered was lower than expected, which impacted the overall tracer distribution and clearance.

These technical challenges highlighted the complexity of IT cannula dosing and suggest that future studies should explore more refined or automated dosing techniques to ensure consistency. Despite these limitations, the initial IT results in young animals confirmed the viability of ^{18}F-FDS for glymphatic studies, though more reliable administration methods are necessary to optimize the approach.

The comparison of administration routes illustrated the clear advantages of intranasal delivery for clinical translation, given its non-invasive nature, ease of administration, and higher brain uptake. While IT injections provided valuable insights into glymphatic clearance, the variability and invasiveness of the method limit its practical use. Future studies should focus on refining IN delivery methods and exploring alternative absorption enhancers to increase tracer uptake and reduce variability.

Overall, the findings demonstrated the potential of ^{18}F-FDS as a PET tracer for glymphatic clearance studies, particularly in the context of age-related decline in glymphatic function. The ability to detect such changes non-invasively through IN administration could have significant implications for diagnosing and monitoring neurodegenerative diseases. Further research is needed to optimize dosing methods and explore the broader applications of ^{18}F-FDS in both preclinical and clinical settings.

4. CONCLUSIONS

4.1. Synthesis of ^{18}F-FDS

As part of this research ^{18}F-FDS was synthesized and evaluated for its utility as a tracer for glymphatic clearance using PET imaging, advancing methods for studying brain clearance mechanisms. By addressing limitations in existing semi-quantitative MRI approaches, this work contributed to both radiochemistry and neuroimaging, demonstrating the potential of PET imaging for precise quantification of glymphatic function.

The synthesis of ^{18}F-FDS from ^{18}F-FDG was efficient and reproducible, with HPLC analysis playing a critical role in confirming product purity and reaction efficiency. The initial method using a mobile phase of 90% MeCN and 10% H_2O effectively differentiated ^{18}F-FDG from ^{18}F-FDS, but optimization with an 80% MeCN and 20% H_2O phase containing 0.1% TFA significantly improved reproducability and reduced analysis time. Consistent retention times and robust separation confirmed the method's reliability, enabling accurate assessment of reaction mixtures and product stability over time. These findings underscore the practicality of the ^{18}F-FDS synthesis method and its adaptability to various research settings. Future work could refine this method by exploring complementary techniques, such as radioTLC.

The practical implications of this study are far-reaching. The streamlined synthesis of ^{18}F-FDS and its successful application in PET imaging highlight its potential to transform research and clinical approaches to studying in-vivo behavior of ^{18}F-FDS. Not only is ^{18}F-FDS an applicable tracer to glymphatic function, but it can also be used to detect certain bacterial infections[44]. Increasing the efficiency and reliability of ^{18}F-FDS synthesis will make research using ^{18}F-FDS more cost-effective and more reporoducible.

4.2. Clearance of ^{18}F-FDS in rats following intrathecal or intranasal delivery

This study aimed to evaluate the potential of ^{18}F-FDS as a PET tracer for assessing glymphatic clearance and to identify the most clinically translatable route of administration. The findings demonstrated that ^{18}F-FDS is an effective tracer for studying glymphatic function, offering quantitative PET imaging metrics that provide consistent and reproducible data for preclinical research. The ability to quantify glymphatic clearance through fold change in tracer concentration, activity per voxel, and total activity within

defined VOIs represents a significant advancement in creating a standardized approach for evaluating this critical physiological pathway. These metrics not only support future comparative studies but also lay the groundwork for diagnostic tools to monitor glymphatic function in both healthy and diseased states.

IT injections served as the primary method for delivering ^{18}F-FDS to the CNS in young animals. These experiments revealed a rapid and detectable clearance of the tracer, with statistically significant reductions in tracer activity at 1.75 and 3 hours post-injection compared to initial imaging at 0.5 hours. This rapid clearance highlights the efficiency of glymphatic function in healthy, young animals.

However, IT injection presented several challenges. Variability in hand-injected doses led to inconsistent tracer delivery to the CNS, reducing the sample size for analysis as animals with insufficient CNS tracer uptake had to be excluded. Even when using surgically implanted ICM cannulas to achieve more controlled IT dosing, technical issues, such as misalignment of syringe pump extenders, resulted in under-delivery of tracer. These challenges emphasized the need for automated or improved manual dosing techniques to ensure accuracy and reproducibility in future studies.

IN administration emerged as a promising non-invasive alternative. Leveraging the N2B pathway, IN delivery facilitated tracer uptake into the CNS without the invasiveness of IT injection. Among the routes tested, IN delivery demonstrated the highest maximum percentage of the injected dose reaching the brain, supporting its potential for clinical applications. However, initial experiments with IN administration were hindered by high variability in tracer uptake and inconsistent results across trials. Formulations of ^{18}F-FDS with DDM and TDM, designed to enhance absorption, did not yield sufficient improvements and were ultimately discontinued. Despite these limitations, the non-invasive nature of IN administration and its capacity for CNS delivery align with existing literature and highlight its suitability for future refinement. Addressing variability through improved formulations and delivery methods will be critical for optimizing IN administration.

By contrast, IV administration confirmed that 18F-FDS is unsuitable for systemic delivery due to its inability to cross the BBB, as expected. This finding underscores the importance of selecting an appropriate route of administration to maximize CNS uptake and highlights the limitations of systemic delivery for this tracer.

Comparative studies between young and aged animals provided additional insights into glymphatic function. Although the small sample size in aged animals precluded statistical analysis, visual comparisons of PET/MR image arrays and fold change trends suggested decreased glymphatic clearance in aged animals. This finding aligns with the hypothesis that glymphatic function declines with age, a phenomenon associated with the accumulation of neurotoxic waste products and the development of neurodegenerative diseases. The observed differences between young and aged animals may indicate that the sensitivity of ^{18}F-FDS PET imaging is sufficient to detect age-related changes in glymphatic activity, offering a potential diagnostic tool for early identification of conditions such as Alzheimer's disease and other dementias.

The study's findings emphasize the importance of refining dosing methods and improving reproducibility to fully realize the potential of ^{18}F-FDS PET imaging. While IT injections provided critical data on glymphatic clearance mechanisms, their invasiveness and technical challenges limit their practicality for widespread application. IN administration offers a more clinically relevant and scalable approach, but further optimization is required to reduce variability and enhance reliability. Future research should focus on developing enhanced IN formulations, exploring alternative absorption enhancers, and employing advanced imaging techniques to validate these methods in larger cohorts.

In addition to optimizing delivery methods, this research highlighted broader implications for the role of glymphatic imaging in understanding and diagnosing neurodegenerative diseases. The ability to non-invasively assess glymphatic clearance through PET imaging has the potential to revolutionize how we detect and monitor conditions associated with glymphatic dysfunction, including Alzheimer's disease, Parkinson's disease, and other age-related neurodegenerative disorders. The differences observed between young and aged animals underscore the importance of studying glymphatic health across the lifespan, with a focus on identifying early biomarkers of disease progression.

In conclusion, this study demonstrated the potential of ^{18}F-FDS as a PET tracer for glymphatic clearance, provided critical insights into the relative strengths and limitations of different administration routes, and highlighted the tracer's sensitivity to age-related

changes in glymphatic function. These findings pave the way for future research aimed at optimizing tracer delivery, expanding preclinical models, and ultimately translating this approach to clinical applications. The development of non-invasive imaging techniques using ^{18}F-FDS could significantly enhance our ability to diagnose, monitor, and treat diseases linked to impaired glymphatic function, offering new avenues for improving brain health and overall quality of life.

REFERENCES

1. Breijyeh, Z. & Karaman, R. Comprehensive Review on Alzheimer's Disease: Causes and Treatment. *Molecules* **25**, 5789 (2020).
2. Kerwin, D.*, et al.* Alzheimer's disease diagnosis and management: Perspectives from around the world. *Alzheimer's & Dementia: Diagnosis, Assessment & Disease Monitoring* **14**, e12334 (2022).
3. Iliff, J.J.*, et al.* A Paravascular Pathway Facilitates CSF Flow Through the Brain Parenchyma and the Clearance of Interstitial Solutes, Including Amyloid β. *Science Translational Medicine* **4**, 147ra111-147ra111 (2012).
4. Rasmussen, M.K., Mestre, H. & Nedergaard, M. Fluid transport in the brain. *Physiological reviews* **102**, 1025-1151 (2022).
5. Ballabh, P., Braun, A. & Nedergaard, M. The blood–brain barrier: an overview: Structure, regulation, and clinical implications. *Neurobiology of Disease* **16**, 1-13 (2004).
6. Lochhead, J.J. & Thorne, R.G. Intranasal delivery of biologics to the central nervous system. *Advanced Drug Delivery Reviews* **64**, 614-628 (2012).
7. Dhuria, S.V., Hanson, L.R. & Frey, W.H., 2nd. Intranasal delivery to the central nervous system: mechanisms and experimental considerations. *J Pharm Sci* **99**, 1654-1673 (2010).
8. Iwasaki, S.*, et al.* Direct Drug Delivery of Low-Permeable Compounds to the Central Nervous System Via Intranasal Administration in Rats and Monkeys. *Pharmaceutical Research* **36**, 76 (2019).
9. Iliff, J.J.*, et al.* Brain-wide pathway for waste clearance captured by contrast-enhanced MRI. *The Journal of Clinical Investigation* **123**, 1299-1309 (2013).
10. Ahsan, F., Arnold, J., Meezan, E. & Pillion, D.J. Enhanced Bioavailability of Calcitonin Formulated with Alkylglycosides Following Nasal and Ocular Administration in Rats. *Pharmaceutical Research* **18**, 1742-1746 (2001).
11. Maggio, E.T. & Pillion, D.J. High efficiency intranasal drug delivery using Intravail® alkylsaccharide absorption enhancers. *Drug Delivery and Translational Research* **3**, 16-25 (2013).
12. Alitalo, K. The lymphatic vasculature in disease. *Nature Medicine* **17**, 1371-1380 (2011).
13. Stephens, M. & von der Weid, P.-Y. Chapter 3 - Lymphatic pumping and pathological consequences of its dysfunction. in *Lymphatic Structure and Function in Health and Disease* (ed. F.N.E. Gavins & J.S. Alexander) 19-54 (Academic Press, 2020).
14. Damkier, H.H., Brown, P.D. & Praetorius, J. Cerebrospinal Fluid Secretion by the Choroid Plexus. *Physiological Reviews* **93**, 1847-1892 (2013).
15. Woollam, D.H.M. & Millen, J.W. PERIVASCULAR SPACES OF THE MAMMALIAN CENTRAL NERVOUS SYSTEM. *Biological Reviews* **29**, 251-283 (1954).
16. Mestre, H.*, et al.* Flow of cerebrospinal fluid is driven by arterial pulsations and is reduced in hypertension. *Nature Communications* **9**, 4878 (2018).

17. Weller, R.O., Subash, M., Preston, S.D., Mazanti, I. & Carare, R.O. Perivascular drainage of amyloid-beta peptides from the brain and its failure in cerebral amyloid angiopathy and Alzheimer's disease. *Brain pathology* **18 2**, 253-266 (2008).

18. Ballatore, C., Lee, V.M.-Y. & Trojanowski, J.Q. Tau-mediated neurodegeneration in Alzheimer's disease and related disorders. *Nature Reviews Neuroscience* **8**, 663-672 (2007).

19. Polymeropoulos, M.H.*, et al.* Mutation in the alpha-synuclein gene identified in families with Parkinson's disease. *Science* **276 5321**, 2045-2047 (1997).

20. Kress, B.T.*, et al.* Impairment of paravascular clearance pathways in the aging brain. *Annals of Neurology* **76**, 845-861 (2014).

21. Xu, Z.*, et al.* Deletion of aquaporin-4 in APP/PS1 mice exacerbates brain Aβ accumulation and memory deficits. *Molecular Neurodegeneration* **10**, 58 (2015).

22. Zou, W.*, et al.* Blocking meningeal lymphatic drainage aggravates Parkinson's disease-like pathology in mice overexpressing mutated α-synuclein. *Translational Neurodegeneration* **8**, 7 (2019).

23. Hablitz, L.M.*, et al.* Increased glymphatic influx is correlated with high EEG delta power and low heart rate in mice under anesthesia. *Science Advances* **5**, eaav5447 (2019).

24. Xie, L.*, et al.* Sleep Drives Metabolite Clearance from the Adult Brain. *Science* **342**, 373-377 (2013).

25. Götz, J., Bodea, L.-G. & Goedert, M. Rodent models for Alzheimer disease. *Nature Reviews Neuroscience* **19**, 583-598 (2018).

26. Mitchell, S.J., Scheibye-Knudsen, M., Longo, D.L. & de Cabo, R. Animal Models of Aging Research: Implications for Human Aging and Age-Related Diseases*. *Annual Review of Animal Biosciences* **3**, 283-303 (2015).

27. Shah, N.J. *Hybrid MR-PET Imaging: Systems, Methods and Applications* (The Royal Society of Chemistry, 2019).

28. Endrikat, J.*, et al.* Clinical Efficacy of Gadobutrol: Review of Over 25 Years of Use Exceeding 100 Million Administrations. *Investigative Radiology* **59**, 345-358 (2024).

29. Magnetic Resonance Imaging Units (per million population), total density. (World Health Organization, 2023).

30. Gulani, V. & Seiberlich, N. Quantitative MRI: Rationale and Challenges. in *Advances in Magnetic Resonance Technology and Applications* xxxvii-li (Academic Press, 2020).

31. Schwenck, J.*, et al.* Advances in PET imaging of cancer. *Nature Reviews Cancer* **23**, 474-490 (2023).

32. Jacobson, O., Kiesewetter, D.O. & Chen, X. Fluorine-18 Radiochemistry, Labeling Strategies and Synthetic Routes. *Bioconjugate Chemistry* **26**, 1-18 (2015).

33. Ward, J., Ly, M. & Raji, C.A. Brain PET Imaging: Frontotemporal Dementia. *PET Clin* **18**, 123-133 (2023).

34. Johnson, K.A., Fox, N.C., Sperling, R.A. & Klunk, W.E. Brain imaging in Alzheimer disease. *Cold Spring Harb Perspect Med* **2**, a006213 (2012).

35. Pemberton, H.G.*, et al.* Quantification of amyloid PET for future clinical use: a state-of-the-art review. *European Journal of Nuclear Medicine and Molecular Imaging* **49**, 3508-3528 (2022).

36. Galant, A.L., Kaufman, R.C. & Wilson, J.D. Glucose: Detection and analysis. *Food Chemistry* **188**, 149-160 (2015).

37. Jandera, P. Stationary and mobile phases in hydrophilic interaction chromatography: a review. *Analytica Chimica Acta* **692**, 1-25 (2011).

38. Ciscato, F., Ferrone, L., Masgras, I., Laquatra, C. & Rasola, A. Hexokinase 2 in Cancer: A Prima Donna Playing Multiple Characters. *International Journal of Molecular Sciences* **22**, 4716 (2021).

39. Li, Z.B.*, et al.* The synthesis of 18F-FDS and its potential application in molecular imaging. *Mol Imaging Biol* **10**, 92-98 (2008).

40. Mota, F., de Jesus, P. & Jain, S.K. Kit-based synthesis of 2-deoxy-2-[18F]-fluoro-d-sorbitol for bacterial imaging. *Nature Protocols* **16**, 5274 - 5286 (2021).

41. Hugon, G.*, et al.* [(18)F]2-Fluoro-2-deoxy-sorbitol PET Imaging for Quantitative Monitoring of Enhanced Blood-Brain Barrier Permeability Induced by Focused Ultrasound. *Pharmaceutics* **13** (2021).

42. Veronesi, M.C.*, et al.* Imaging of intranasal drug delivery to the brain. *Am J Nucl Med Mol Imaging* **10**, 1-31 (2020).

43. Gileta, A.F.*, et al.* Genetic characterization of outbred Sprague Dawley rats and utility for genome-wide association studies. *PLoS Genet* **18**, e1010234 (2022).

44. Yao, S.*, et al.* Infection Imaging With (18)F-FDS and First-in-Human Evaluation. *Nucl Med Biol* **43**, 206-214 (2016).